POLITECNICO DI TORINO
Repository ISTITUZIONALE

Unveiling the synergistic role of anatase/brookite homojunctions in TiO2 mixed phases on the enhanced photocatalytic degradation of paracetamol under simulated solar light and

Original
Unveiling the synergistic role of anatase/brookite homojunctions in TiO2 mixed phases on the enhanced photocatalytic degradation of paracetamol under simulated solar light and the formation of CO2. radical ion / Blangetti, N., Freyria, F.S., Manzoli, M., Rivolo, P., Piovano, A., Darjazi, H., Ditaranto, N., Patrizi, B., Doria, S., Bonelli, B.. - In: APPLIED SURFACE SCIENCE ADVANCES. - ISSN 2666-5239. - 30:(2025). [10.1016/j.apsadv.2025.100896]

Availability:
This version is available at: 11583/3005912 since: 2025-12-16T11:49:07Z

Publisher:
Elsevier

Published
DOI:10.1016/j.apsadv.2025.100896

Terms of use:

This article is made available under terms and conditions as specified in the corresponding bibliographic description in the repository

Publisher copyright

(Article begins on next page)

09 September 2026

Applied Surface Science Advances 30 (2025) 100896

Contents lists available at ScienceDirect

Applied Surface Science Advances

journal homepage: www.sciencedirect.com/journal/applied-surface-science-advances

Full Length Article

Unveiling the synergistic role of anatase/brookite homojunctions in TiO_2 mixed phases on the enhanced photocatalytic degradation of paracetamol under simulated solar light and the formation of $CO_2^{\cdot-}$ radical ion

Nicola Blangetti [a], Francesca S. Freyria [a,*], Maela Manzoli [b], Paola Rivolo [a], Alessandro Piovano [c,d], Hamideh Darjazi [c,d], Nicoletta Ditaranto [e], Barbara Patrizi [f,g], Sandra Doria [g,h], Barbara Bonelli [a,i,*]

[a] Dipartimento di Scienza Applicata e Tecnologia and INSTM Unit of Torino –Politecnico di Torino, Corso Duca degli Abruzzi 24, I-10129 Torino, Italy
[b] Dipartimento di Scienza e Tecnologia del Farmaco and NIS - Centre for Nanostructured Interfaces and Surfaces, University of Turin, Via P. Giuria 9, I-10125 Torino, Italy
[c] GAME Lab – Department of Applied Science and Technology (DISAT), Politecnico di Torino, Corso Duca Degli Abruzzi 24, Torino 10129, Italy
[d] National Reference Centre for Electrochemical Energy Storage (GISEL) – INSTM, Via G. Giusti 9, Firenze, 50121, Italy
[e] Dipartimento di Chimica, Università degli Studi di Bari Aldo Moro, 70125 Bari, Italy
[f] CNR-INO, National Institute of Optics, National Research Council of Italy, Via Madonna del Piano 10, 50019 Sesto Fiorentino, FI, Italy
[g] LENS, European Laboratory for Non Linear Spectroscopy, Via Nello Carrara 1, 50019 Sesto Fiorentino, FI, Italy
[h] ICCOM-CNR, Institute of Chemistry of OrganoMetallic Compounds, National Research Council of Italy Via Madonna del Piano, 10 50019 Sesto Fiorentino (Florence) Italy
[i] Interdepartmental Center PolitoBIOMed, Politecnico di Torino, Corso Duca degli Abruzzi 24, I-10129 Torino, Italy

ARTICLE INFO

Keywords:
TiO_2 polymorphs
Homojunctions
Brookite
Solar photocatalysis
Emerging contaminants
$CO_2^{\cdot-}$ radical ion
Surface-Enhanced Raman Spectroscopy

ABSTRACT

Mixed-phase TiO_2 systems offer unique opportunities for enhancing photocatalytic performance via inter-polymorph junctions (homojunctions). While anatase/rutile interfaces have been extensively studied, anatase/brookite junctions remain comparatively underexplored. Here, we demonstrate that homojunctions between anatase and brookite, formed via a template-free, pH-controlled synthesis and low-temperature calcination (200 °C), significantly enhance photocatalytic activity under simulated solar light. High-resolution TEM reveals direct anatase/brookite junctions without isolated brookite crystallites. At the same time, IR spectroscopy detects the formation of $CO_2^{\cdot-}$ radical ions, suggesting that the homojunctions act as active defect sites, potentially contributing to visible light absorption or increasing photocatalytic performance. Notably, the surface generation of $CO_2^{\cdot-}$ under mild conditions could open new perspectives for CO_2 activation and solar fuel production, while also positioning this species as a valuable intermediate in organic synthesis for the formation of carboxylic acids. Compared to an anatase/brookite/rutile system obtained through calcination at 600 °C, the sample calcined at low temperature exhibits superior performance in degrading paracetamol, a model emerging contaminant in city water. Importantly, Surface-Enhanced Raman Spectroscopy (SERS) enables direct identification of paracetamol degradation intermediates, revealing a mechanistic pathway similar to that promoted by a commercial anatase/rutile TiO_2. These findings underscore the potential of anatase/brookite homojunctions as efficient charge-separating interfaces, as further supported by electrochemical impedance spectroscopy.

1. Introduction

Titanium dioxide (TiO_2) is widely recognized as a highly effective photocatalyst due to its low toxicity, chemical stability, and affordability [1–4]. Among the eight known polymorphic structures of TiO_2, anatase, rutile, and brookite are the most extensively studied crystalline phases [5].

Anatase, an indirect semiconductor with an average band gap energy of approximately 3.2 eV, is typically considered the most active phase for photocatalytic applications, especially when it is prepared in

* Corresponding authors.
E-mail addresses: francesca.freyria@polito.it (F.S. Freyria), barbara.bonelli@polito.it (B. Bonelli).

https://doi.org/10.1016/j.apsadv.2025.100896
Received 27 June 2025; Received in revised form 20 October 2025; Accepted 3 November 2025
Available online 10 November 2025
2666-5239/© 2025 The Author(s). Published by Elsevier B.V. This is an open access article under the CC BY-NC-ND license (http://creativecommons.org/licenses/by-nc-nd/4.0/).

nanostructured forms [1–4]. This is attributed to its high surface area and indirect band gap, hindering electron-hole recombination [1–4].

Rutile, a direct semiconductor with a band gap energy of approximately 3.0 eV, exhibits lower photocatalytic activity due to its generally larger crystallites, resulting in a lower surface area and faster electron-hole recombination rates associated with its direct band gap [1–4].

Brookite, a direct semiconductor with a band gap energy ranging from 3.1 to 3.4 eV, is still underexploited in photocatalysis due to challenges in synthesizing single-phase samples [6–10].

TiO_2 as a photocatalyst faces two primary limitations: i) limited exploitation of solar light, as TiO_2 primarily absorbs in the UV range, which constitutes only 4–5 % of total solar radiation [10], and ii) rapid recombination of photogenerated electrons and holes, which reduces the efficiency of the photocatalytic process [11]. To address these limitations, various strategies have been employed to enhance the photocatalytic efficiency of TiO_2 under solar light, such as the formation of composites [12] and heterojunctions (i.e., junctions between semiconductor materials featuring different band gaps, thus able to maintain the spatial charge separation by accumulating the charge carriers into different electronic bands) [13,14], self-doping [15], and doping with heteroatoms [16–19]. Doping with heteroatoms is a common approach for extending the absorption edge of TiO_2 toward the visible range. However, it can introduce defects that can act as recombination centres for photogenerated electrons and holes [17].

Homojunctions, i.e., junctions between different TiO_2 polymorphs [20], have emerged as a promising strategy for enhancing photocatalytic activity, particularly in utilizing the UV portion of solar irradiation, because they can facilitate charge carrier separation and offer improved structural compatibility due to their identical chemical composition, which minimizes lattice mismatch, lowers interfacial strain, and facilitates band alignment [21]. Anatase/rutile homojunctions are the most extensively studied [15,22]. For example, Degussa P25, a flame-made, widely used commercial TiO_2 photocatalyst, consists of anatase and rutile phases: some rutile nanoparticles form Type II homojunctions on the surface of anatase nanoparticles (Scheme 1b) [22–24], and the remaining ones coexist as single nanoparticles. Although the exact role of anatase/rutile homojunctions in Degussa P25 is still debated [22], they are generally believed to enhance photocatalytic activity, especially by facilitating the separation of charge carriers [25–27].

In contrast to anatase and rutile, the investigation of anatase/brookite mixed phases remains underexplored. Nanocomposites containing anatase/brookite mixed phases can enhance visible light-induced H_2 production [31]. Some of us demonstrated that undoped and Fe-doped anatase/brookite mixed phases exhibit promising performance in the photocatalytic degradation of simazine [32] (a persistent water contaminant), and that undoped TiO_2 anatase/brookite mixed phases efficiently degrade N-phenylurea (another persistent micropollutant) under both UV and solar illumination [33]. The efficient degradation of ibuprofen by a mesoporous anatase/brookite sample under UV light has been attributed to the synergy between anatase and brookite; still, the presence of homojunctions has not been demonstrated [34]. The antibacterial activity of doped anatase/brookite nanojunctions has also been investigated [35]. Still, papers demonstrating the actual occurrence of anatase/brookite homojunctions in undoped TiO_2 are uncommon [37], and their synergistic role in photocatalytic applications remains underexplored.

This study aims to elucidate the role of anatase/brookite homojunctions in photocatalysis by synthesizing two undoped TiO_2 samples using a simple, template-free sol-gel synthesis method. A low temperature calcination (200 °C) yields an anatase/brookite mixed phase, while a higher calcination temperature (600 °C) produces an anatase/brookite/rutile mixed phase. A combination of physicochemical techniques is used to comprehensively characterize the structural and surface properties of the synthesized samples. Electrochemical Impedance Spectroscopy (EIS) is used to elucidate the mechanisms of charge carrier stabilization.

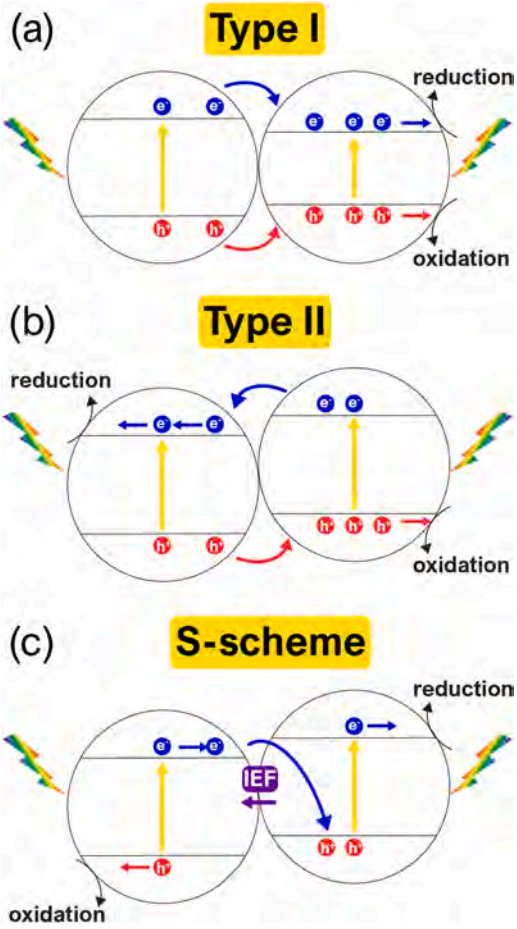

Scheme 1. Possible band alignments in TiO_2 mixed polymorph phases, adapted from refs [28–30]: Type I (a), Type II (b), S-scheme (also known as Z direct-scheme) homojunctions (c, where IEF stands for the Internal Electric Field that is generated at the interface between the two semiconductors, facilitating the efficient transfer of electrons and holes, leading to enhanced photocatalytic activity).

To assess their photocatalytic performance under simulated solar light, we selected the degradation of paracetamol (N-(4-hydroxyphenyl) acetamide) as a model reaction for the removal of emerging pollutants [36–38]. These micropollutants, often present at trace concentrations (from a few ng L^{-1} to several μg L^{-1}), are of increasing environmental concern due to their persistence, poor removal by conventional wastewater treatment, widespread occurrence in aquatic systems, and potential adverse effects on human health and ecosystems [39–43]. Paracetamol, as a commonly used analgesic and antipyretic medication, is frequently detected worldwide in aquatic environments, even in drinking water, making it a relevant target compound [40,44]. Surface-enhanced Raman Spectroscopy (SERS) is employed to identify the potential degradation pathway of paracetamol by detecting reaction products and comparing the results with those reported in the literature, as summarized in Scheme 2 [45,46].

Beyond pollutant removal, photocatalytically active TiO_2 systems are gaining interest for their ability to generate reactive radical species with broader chemical relevance. Among these, the carbon dioxide radical anion ($CO_2^{\bullet-}$) is of particular importance. This highly reactive, nucleophilic species has been recognized not only as a key intermediate in the initial step of CO_2 photoreduction, an essential reaction in the pursuit of solar fuels, but also as an effective single-electron donor in organic synthesis [47]. While its direct generation from CO_2 is challenging due to the molecule's high reduction potential, we will show that the formation of $CO_2^{\bullet-}$ can be promoted under mild conditions on the surface of TiO_2,

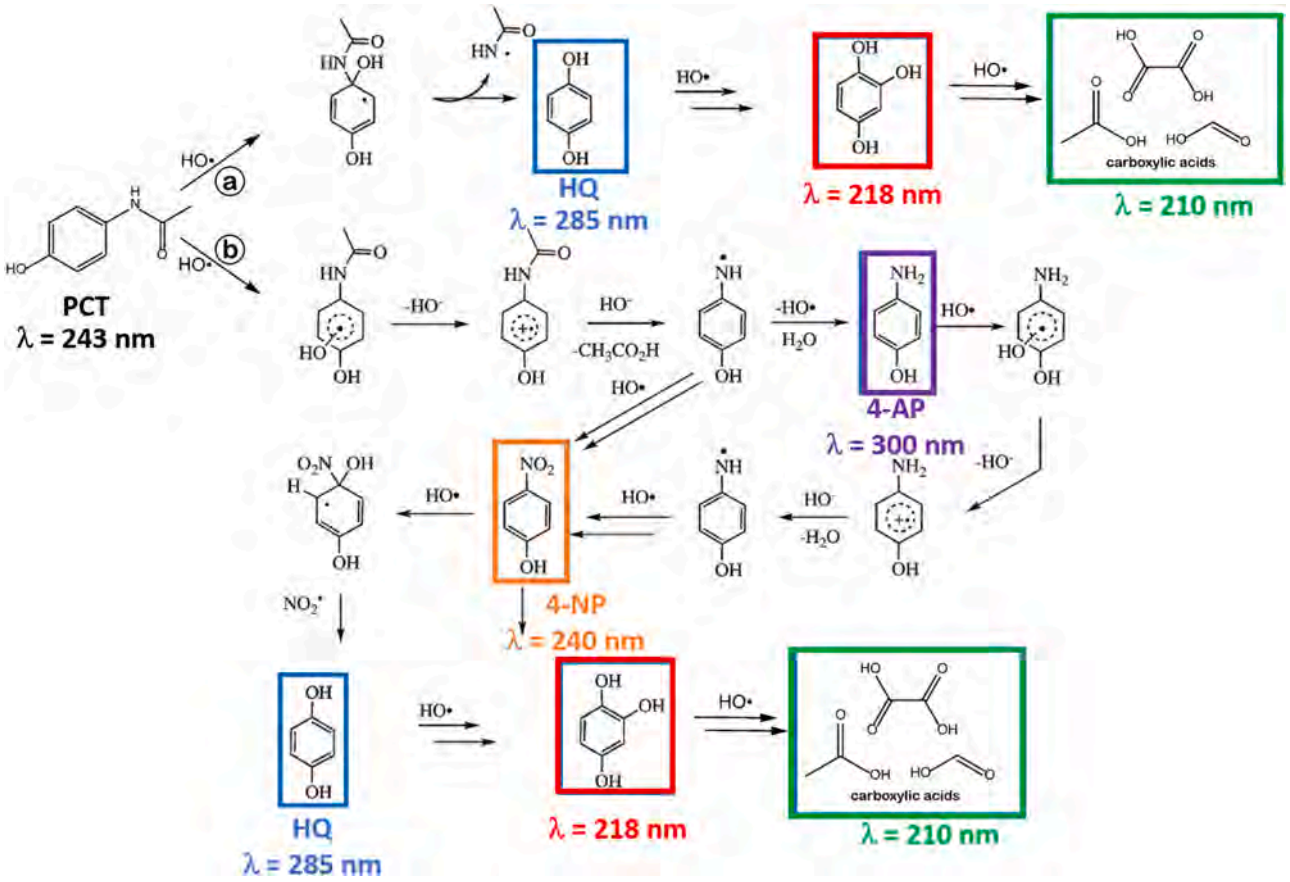

Scheme 2. The two degradation pathways of paracetamol (PCT) acknowledged by the literature, adapted from refs [45,46]. The compounds in the boxes correspond to possible by-products that may form during the experiments in Fig. 9, as indicated by the observed UV absorption bands at the specified wavelengths. The SERS analysis focuses on the detection of hydroquinone (HQ), 4-aminophenol (4-AP), and 4-nitrophenol (4-NP).

particularly in the presence of anatase/brookite homojunctions, suggesting the presence of surface defects or active sites favorable for this transformation.

2. Experimental section

2.1. Materials synthesis

All reagents used for the syntheses were ACS-grade chemicals purchased from Merck.

The anatase/brookite (AB sample, A: anatase, B: brookite) and anatase/brookite/rutile (ABR sample; R: rutile) TiO_2 mixed phases were synthesized using a template-free sol-gel method under pH control to tune the brookite formation. The synthesis procedure was adapted by modifying the process initially developed by Mutuma et al. slightly [48], which allows the formation of homojunctions and is described as follows. A solution was prepared by mixing 30.0 mL of titanium(IV) isopropoxide ($Ti(OPr)_4$) with 30.0 mL of isopropanol in a 150 mL beaker. The solution was stirred at 500 rpm for 20 min, followed by the addition of 300 mL of double-distilled water while stirring. The resulting mixture was transferred to a Teflon autoclave and heated at 80 °C for 5 h in a stove. After heating, the mixture cooled down to room temperature. The pH of the yellowish solution was adjusted to 2.0 by the dropwise addition of 1.0 M HNO_3 solution. This pH value was chosen based on the paper by Mutuma et al. [48], indicating the highest brookite mass percentage of 20 % at this pH.

The sol was stirred at room temperature for 20 h to form a gel. The gel was washed several times with double-distilled water and isopropyl alcohol, followed by centrifugation at 4000 rpm for 12 min. The obtained precipitate was dried in a drying oven with natural convection (Binder ED-53) at 100 °C for 12 h. The dried product was divided into two aliquots. The former was calcined in a muffle furnace (Ney Vulcan 3–550) at 200 °C for 2 h (AB sample), and the latter was calcined at 600 °C for 2 h (ABR sample), both with a temperature ramp of 5 °C min^{-1} before cooling to room temperature. Both calcined powders were washed four times with an ethanol/water (1/3) mixture, centrifuged at 8000 rpm for 10 min, and dried at 60 °C for 24 h.

2.2. Physicochemical characterization methods

X-ray powder diffraction (XRD) patterns were collected using an X'Pert Philips PW3040 diffractometer with Cu K_α radiation (2θ range = 10°–100°; step=0.026° 2θ; time per step = 0.8 s). The XRD patterns were indexed by referencing the Powder Diffraction File database (PDF 20,002,004, International Centre for Diffraction Data, Pennsylvania) and the Crystallography Open Database (COD 2013). Quantitative Phase Analysis (QPA) was made by applying the full-profile Rietveld method to the diffraction patterns using X'Pert High Score Plus 3.0e software. The crystallite average size (D) was determined using the Williamson-Hall plot, calculated by the X'Pert High Score Plus 3.0e software.

N_2 adsorption/desorption isotherms were measured at −196 °C using a Micromeritics ASAP 2020Plus instrument. Before analysis, powders were pre-outgassed at 150 °C for 4 h to remove water and other atmospheric contaminants. The Specific Surface Area (SSA) was calculated using the Brunauer-Emmett-Teller (BET) method.

High-resolution transmission electron microscopy (HRTEM) characterization was performed using a side-entry JEOL (Akishima, Tokyo, Japan) JEM-3010 UHR microscope (300 kV, LaB_6 filament). All digital

micrographs were acquired using an UltraScan 1000 camera, and the images were processed using Gatan Digital Micrograph software (Pleasanton, CA, USA). For HRTEM analysis, a small amount of powder (2–3 mg) was sonicated in isopropanol and transferred as a suspension to a copper grid covered with a holey carbon film.

Particle size distributions were obtained by counting a statistically representative number of particles for each sample (>150 particles).

The mean particle diameter (d_m) was calculated using the equation $d_m = \Sigma d_i n_i / \Sigma n_i$, where n_i is the number of particles with diameter d_i.

The presence of homojunctions was investigated by analyzing the interplanar spacings measured from the Fast Fourier Transform (FFT) of all the HRTEM images collected for each sample.

Raman spectroscopic characterization was performed using a Renishaw InVia Reflex micro-Raman spectrometer (Renishaw plc, Wotton-under-Edge, UK), equipped with a cooled charge-coupled device (CCD) camera as the detector and a diode laser ($\lambda_{ex} = 514.5$ nm) as the excitation source. The powder samples were pressed onto a microscope glass slide to ensure the required flatness for inspection using several microscope objectives for backscattering light collection. A 20x objective, 1 mW laser power, 3 s exposure time, and 3 accumulations were the settings applied for the spectral acquisitions on the TiO_2 samples. The Raman spectra of paracetamol, hydroquinone, 4-aminophenol, and 4-nitrophenol powders were registered using a 20x objective, 0.1 mW laser power, 10 s exposure time, and 1 accumulation on the pure reagents purchased from Merck. The conditions configured for the SERS spectra acquisition are reported in Section 2.4.

The TiO_2-based electrodes for electrochemical impedance spectroscopy (EIS) measurements were prepared under ambient laboratory conditions; all chemicals, except those used in the TiO_2 materials under study, were sourced from Merck. In detail, polyvinylidene fluoride (PVDF) was dissolved in N-methyl pyrrolidone (NMP) under continuous stirring until a clear solution was obtained. The active materials and conductive carbon (Super C65, Timcal) were dry-mixed and ground before being incorporated into the prepared solution. This process yielded slurries with a mass ratio of active material: Super C65: binder of 70:20:10. Stirring continued for 6 h to achieve uniformity. The resulting dense slurries were cast onto nickel (Ni) foils as current collectors using a doctor blade to ensure a consistent wet film thickness of 300 μm. The coated electrodes were then dried at 80 °C, and discs (2.54 cm^2 area) were cut out of the dry electrode film for cell assembly and testing. Two identical disc electrodes were assembled in a symmetrical $TiO_2 \| TiO_2$ cell configuration, housed in an ECC-Std electrochemical test cell (EL-Cell, Germany), separated by a Whatman GF/A separator soaked in a 1 M aqueous solution of NaCl electrolyte.

EIS measurements were conducted at ambient temperature in the frequency range between 300 kHz and 1 Hz. The Nyquist plots obtained from the EIS measurements were curve-fitted by applying the equivalent circuit model shown in the lower inset of Fig. 5. In this model, R_1 represents the liquid electrolyte resistance, R_2 corresponds to the resistance towards charge transfer in TiO_2 (namely, the exchange of ions and the associated movement of electrons), C_{dl} denotes the double-layer capacitance, W accounts for Warburg impedance, which is related to diffusion processes, and, finally, C_i is the intercalation capacity. To account for deviations from ideal behavior due to electrode inhomogeneity or roughness, all C elements were replaced with constant-phase elements (Q) in the fitting procedure. This process was performed using RelaxIS software by rhd instruments GmbH [49,50].

Photoluminescence (PL) spectra were recorded using an Edinburgh Instruments FLS1000 spectrofluorometer equipped with a xenon arc lamp as the excitation source and a photomultiplier tube detector. The samples were prepared by drop-casting ethanol dispersions of the powders onto CaF_2 windows (1 inch diameter, 1 mm thickness) and drying under ambient conditions. Measurements were performed at room temperature using excitation wavelengths of 350 nm, corresponding to near-band-edge excitation. The emission spectra were collected in the 380–700 nm range, with slit widths and integration times optimized for a high signal-to-noise ratio. All the spectra were corrected for the instrumental response, and identical measurement conditions were applied to all the studied samples to enable reliable comparison of their photoluminescence intensity and spectral features. The photoluminescence quantum yield (PLQY) of each sample was tentatively measured (vide infra) using the QYPro™ Integrating Sphere accessory (Edinburgh Instruments) coupled to the same FLS1000 system. Measurements were performed under identical excitation conditions, and the PLQY values were calculated automatically by the instrument software based on the ratio of emitted to absorbed photons, following the manufacturer's calibration and correction procedures.

Diffuse Reflectance (DR) UV–Vis spectra of the powder samples were measured using a Cary 5000 UV–Vis-NIR spectrophotometer (Varian instruments) equipped with a DR sphere.

X-ray photoelectron Spectroscopy (XPS) analysis was performed using a PHI 5000 VersaProbe (Physical Electronics) instrument with monochromatic Al K_α radiation (1486.6 eV energy) as the X-ray source. Two different pass energy values were used: 187.75 eV for survey spectra and 23.5 eV for high-resolution (HR) spectra. The spectral line shift of the C 1 s binding energy (BE) value at 284.8 eV was used to correct for any sample charging effects. Data processing was performed using MultiPak software (v. 9.8.0.19).

For IR measurements, powders were pressed into thin, self-supporting wafers (approximately 8 mg cm^{-2}) and outgassed at 100, 200, and 300 °C. Each outgassing step was conducted for 1 h in a custom-made quartz cell equipped with IR-transparent KBr windows. IR spectra were recorded at a 2 cm-1 resolution using a Bruker EQUINOX-66 spectrometer equipped with a mercury-cadmium-telluride (MCT) cryodetector.

ζ-potential curves were obtained by measuring the electrophoretic mobility as a function of pH using dynamic light scattering (DLS) on a Zetasizer Nano-ZS (Malvern Instruments, Worcestershire, UK). Powders were suspended in ultrapure water and sonicated for 2 min (10 W/mL, 20 kHz, Sonoplus, Bandelin, Berlin, Germany), followed by 5 min of magnetic stirring. pH was adjusted by adding either 0.1 M NaOH or 0.1 M HCl.

2.3. Photocatalytic tests

For the photocatalytic tests, a catalyst concentration of 1.0 g L^{-1} or 0.15 g L^{-1} was added to 50 mL of a 0.01 mM aqueous paracetamol solution. The mixtures were left to equilibrate in dark conditions for 1 h before starting the photocatalytic tests. This step was taken to assess the extent of paracetamol adsorption onto the catalyst surface in the absence of light. The natural pH of the paracetamol solution was 5.7. At this pH, the paracetamol molecule is neutral ($pK_a = 9.5$).

Photocatalytic experiments were performed under simulated solar light (AM 1.5 G, 100 mW cm^{-2}) obtained using a plasma lamp (LIFI STA-40, LUXIM, Santa Clara, CA, USA). The illumination conditions corresponded to 1 Sun, with the following irradiances: ~1000 W m^{-2} in the 400–1050 nm range, ~21 W m^{-2} in the UVA range (315–400 nm) and 44×10^{-3} W m^{-2} in the UVB range (280–315 nm).

The liquid/solid suspension inside the testing tube was continuously stirred at approximately 300 rpm using a magnetic stirrer to ensure proper mixing and contact between the powder(s) and the paracetamol solution.

The reaction mixture was not de-aerated, allowing atmospheric O_2 to be present throughout the photocatalytic tests. Aliquots of the suspension were collected at regular time intervals during the photocatalytic tests. The suspended photocatalyst particles were separated by centrifugation at 12,000 rpm for 12 min using a Thermo Fisher centrifuge. UV–Vis spectra of the supernatant solutions were measured in the 190–800 nm range using a Cary 5000 UV–Vis-NIR spectrophotometer.

Blank experiments, conducted without any photocatalyst, were performed using a 0.01 mM aqueous paracetamol solution to verify the absence of mere photolysis under the same illumination conditions. The

results of these control experiments are shown in **Figure S.1**.

2.4. Surface-Enhanced raman spectroscopy (SERS)

SERS spectra were recorded using the same apparatus as that used for the Raman characterization of powders, as described in Section 2.2. 10 μL of the supernatant solutions obtained after 1 h of reaction in the presence of 0.15 g L^{-1} and 1 g L^{-1} of AB were dropped onto a SERS substrate, namely an Ag-porous silicon (pSi)-polydimethylsiloxane (PDMS) membrane freshly prepared according to a previously reported procedure [51]. Reference aqueous solutions of the pure reagents (paracetamol, hydroquinone, 4-aminophenol, and 4-nitrophenol) were prepared at a concentration of 100 mM and dropped onto the SERS substrates. Before the measurements, all the samples were left to air-dry at room temperature. A 20x objective was used to collect single spectra on the SERS substrates spotted with the reference solutions and the 1 g L^{-1} supernatant aliquots. In contrast, a 50x objective was employed for the measurements on the SERS substrates spotted with the 0.15 g L^{-1} supernatant aliquots. The laser power (100 mW) was reduced to 1 % of the original power through neutral density filters. Each spectral acquisition lasted 3 s, subdivided into three accumulations. To minimize the local power density and prevent sample degradation, a 5 % defocalization of the laser spot was applied. Average SERS spectra were subsequently generated, and baseline correction was performed utilizing the Wire 5.1 software.

3. Results and discussion

3.1. Physicochemical properties of the materials under study

3.1.1. Structural and textural properties

Fig. 1a shows the powder XRD patterns of the AB and ABR samples. The peaks in the patterns are indexed to the anatase (A, PDF 01–078–2486), brookite (B, COD 96–900–4141), and rutile (R, PDF 01–073–1782) polymorphs of TiO_2; for clarity, only the main peaks of the three polymorphs are labeled in the Figure.

Table 1 summarizes the QPA results, along with crystallite size information. Both the AB and the ABR samples are mixed phases. AB is an anatase/brookite mixture (78.0 % anatase and 22.0 % brookite), with a very small average crystallite size (5.5 ± 0.6 nm for anatase and 3.8 ± 0.4 nm for brookite). ABR is an anatase/brookite/rutile mixture (84.6 % anatase, 10.5 % brookite, and 4.90 % rutile) with larger crystallite size (39 ± 5.5 nm for anatase, 16.8 ± 3.6 nm for brookite, and 52.1 ± 8.1 nm for rutile). The higher calcination temperature (600 °C) of ABR results in the formation of rutile and a significant increase in the crystallite size of all phases, as expected. According to the literature, the presence of brookite in these anatase/brookite mixed phases synthesized at acidic pH [52] likely favours the formation of rutile upon calcination at 600 °C.

Fig. 1b reports the N_2 adsorption/desorption isotherms measured at −196 °C, which are used to analyze the surface area and porosity of the samples. Both AB and ABR exhibit type IV isotherms [53,54] with H2 hysteresis loops, indicating the presence of mesopores. The AB sample, calcined at a lower temperature (200 °C), has a significantly higher BET SSA of 210 $m^2\ g^{-1}$ and a larger pore volume (0.31 $cm^3\ g^{-1}$) compared to the ABR sample (BET SSA of 31 $m^2\ g^{-1}$ and pore volume of 0.11 $cm^3\ g^{-1}$). The higher SSA of AB is attributed to its smaller crystallite size and the presence of primarily interparticle mesopores resulting from the sol-gel synthesis and low-temperature calcination (200 °C). The lower SSA of ABR is due to the higher calcination temperature, which promotes crystallite growth and the formation of larger nanoparticles, in agreement with XRD analysis (Table 1). The presence of rutile, known for its higher density and larger particle size, also contributes to the lower SSA of this sample.

TEM analysis (Fig. 2) shows that the AB powder consists of small, roundish crystalline nanoparticles in the tetragonal anatase phase (JCPDS file number 00–001–0562) and in the orthorhombic brookite

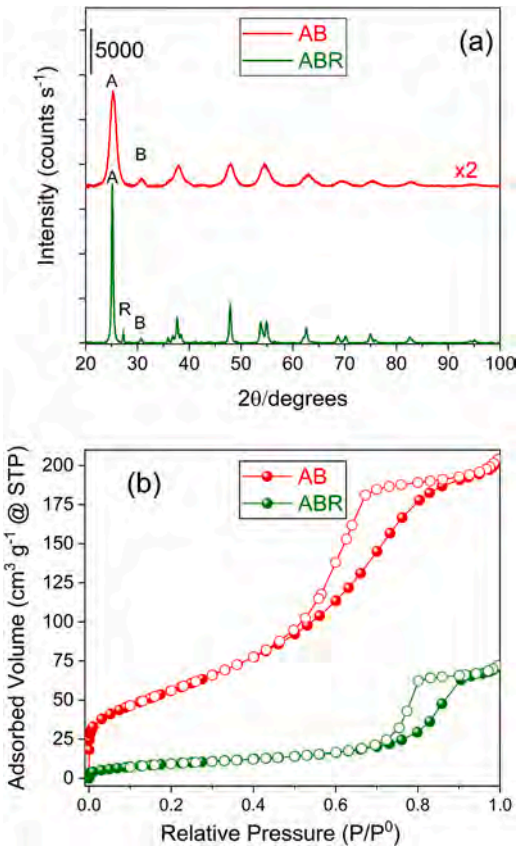

Fig. 1. Powder XRD patterns (a) and N_2 isotherms at −196 °C (b) of the AB (red) and ABR (green) samples. In panel (a), only the main peaks of anatase (A), rutile (R), and brookite (B) are labeled, and the XRD patterns of AB have been multiplied for a better comparison.

Table 1
Crystallite size (from Williamson-Hall plot) and QPA results (as obtained by Rietveld refinements of the XRD patterns reported in Fig. 1a); BET SSA values and Total Pore Volumes (as obtained from N_2 isotherms at – 196 °C shown in Fig. 1b).

Sample	Crystallite size (nm)	QPA results (wt. %)	BET SSA ($m^2\ g^{-1}$) Total Pore Volume ($cm^3\ g^{-1}$)
AB	5.5 ± 0.6 (A)	78.0 (A)	210
	3.8 ± 0.4 (B)	22.0 (B)	0.31
ABR	39 ± 5.5 (A)	84.6 (A)	31
	16.8 ± 3.6 (B)	10.5 (B)	
	52.1 ± 8.1 (R)	4.90 (R)	0.11

phase (JCPDS file number 00–003–0380). The nanoparticles have a roundish shape and an average diameter (d_m) equal to 5.2 ± 1.7 nm, the majority of them having a size between 4 and 5 nm (Fig. 2a).

Conversely, as shown in Fig. 2b, the ABR sample contains larger crystallites with a square shape and a heterogeneous size, as indicated by the very broad particle size distribution, which results in an average diameter of 24.1 ± 12.5 nm, in agreement with the low SSA of the sample (Table 1). In addition to the presence of both anatase and brookite phases, some particles in the tetragonal rutile phase (JCPDS file number 00–001–1292) are also observed (data not shown), in agreement with the sample's XRD pattern.

A detailed analysis of the HRTEM results for the AB and ABR samples was performed, as mixed phases can lead to the formation of homojunctions [27,55]. Their presence is significant as they can influence the photocatalytic properties by affecting charge carrier separation and

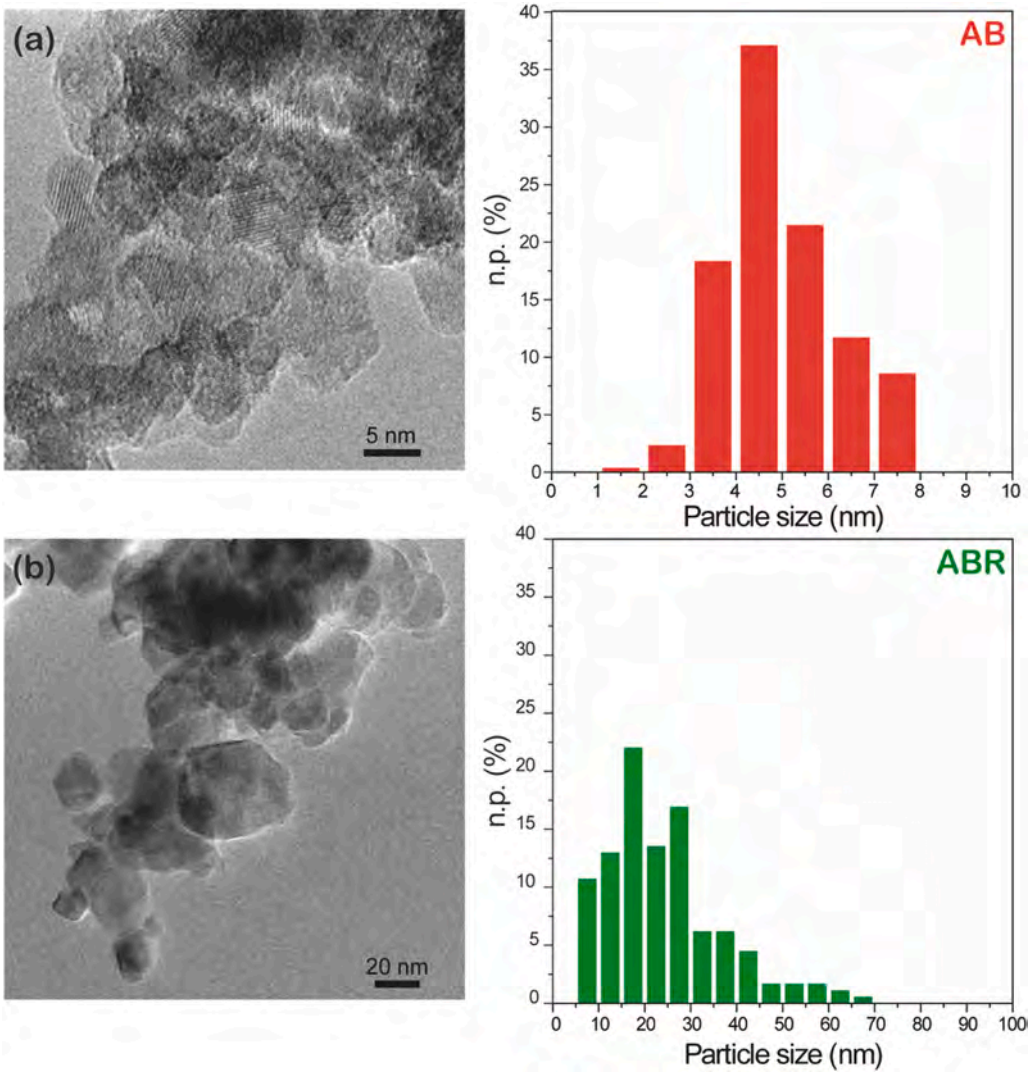

Fig. 2. Representative TEM images and corresponding particle size distributions of AB (a) and ABR samples (b). The instrumental magnification was 500,000 × and 100,000 × in sections (a) and (b), respectively.

recombination processes. Selected micrographs are presented in Fig. 3, where the presence of anatase/brookite homojunctions, observed in the case of the AB sample, is shown and highlighted by red circles (Fig. 3a and 3b). Fig. 3b and 3e show measured lattice fringe spacings of 3.52 Å and 2.90 Å, consistent with the $d_{(101)}$ plane of anatase and the $d_{(121)}$ plane of brookite, respectively. For clarity, each image is accompanied by the corresponding Fast Fourier Transform (FFT) image, which helps identify the diffraction spots associated with each crystalline phase. The number of anatase/brookite homojunctions is estimated to reach about 32 % of the total acquired HRTEM images.

Interestingly, this type of junction is also detected in the ABR sample, in agreement with the QPA results in Table 1. In this case, the larger size of the TiO_2 particles facilitates the observation of such defects, highlighted by a green circle in Fig. 3g Nevertheless, homojunctions are observed in 19 % of the acquired images. In Fig. 3h, the lattice fringe spacings are 3.52 Å (consistent with the $d_{(101)}$ plane of anatase), 2.90 Å, and 2.11 Å (consistent with the $d_{(121)}$ and $d_{(140)}$ planes of brookite, respectively). Considering that according to the QPA (Table 1), the amount of brookite in the AB powder corresponds to 22.0 %, this suggests that the occurrence of single-phase brookite nanoparticles is unlikely and that the adopted synthesis favors the formation of anatase/brookite homojunctions, rather than separate phases. TEM/HRTEM characterization reveals distinct differences in particle size between the AB and ABR samples, confirming the presence of crystalline phases identified by XRD.

The Raman spectrum of the AB powder reported in Fig. 4 allows for the identification of the characteristic peaks of both anatase and brookite: the most intense anatase spectral feature at 143 cm^{-1} (E_g mode) [56,57] is superimposed on the most intense and broad brookite one centred at 151 cm^{-1} (A_{1g} mode) [58].

Other intense peaks ascribable to anatase are observable at about 400 cm^{-1} (B_{1g} mode), 517 cm^{-1} (A_{1g} mode), and 638 cm^{-1} (E_g mode). Among the less intense ones, only the E_g mode at 197 cm^{-1} is distinctly visible. The less intense peaks observable at approximately 245 cm^{-1} (A_{1g} mode), in the 282–288 cm^{-1} range (B_{3g} mode), at 325 cm^{-1} (B_{1g} mode), 366 and 584 cm^{-1} (B_{2g} modes), and 451 cm^{-1} (A_{1g} mode) are related to brookite. Interestingly, Zhao et al. [59] observed the same mixed Raman features in a TiO_2 sample with an anatase/brookite mass ratio of approximately 75/25 (similar to that of AB, Table 1).

In the Raman spectrum of the ABR sample, in addition to the anatase and brookite peaks, some spectral features characteristic of rutile are also present. Therefore, the spectrum interpretation may be more complex due to the proximity of some Raman peaks. The B_{1g} mode of rutile is centred at 145 cm^{-1}; this peak is often weak in anatase-rich mixtures and may overlap with the corresponding anatase mode. The same occurs with the 235 cm^{-1} peak (due to a two-phonon scattering

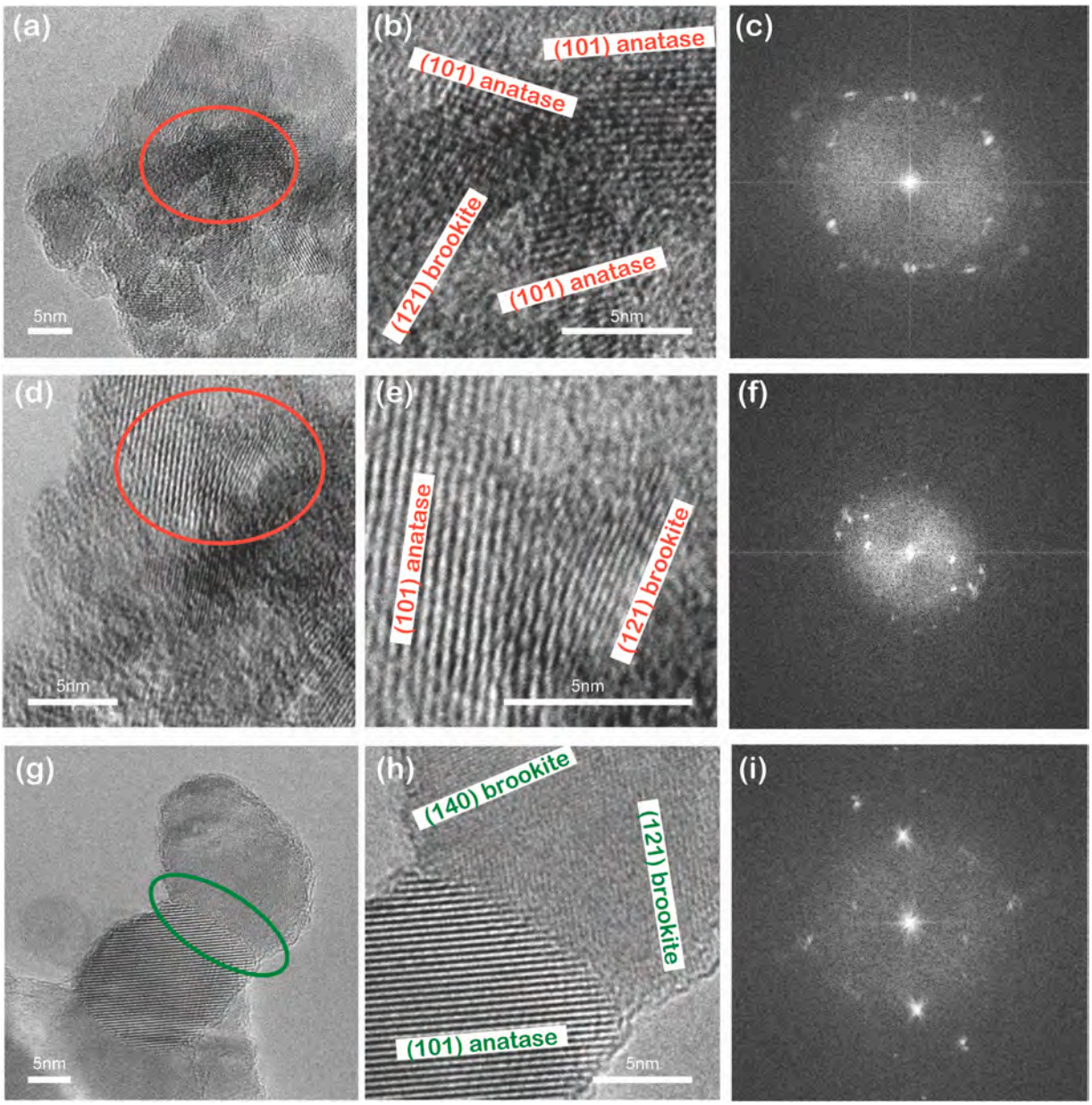

Fig. 3. Representative HRTEM images (a and d) of the AB sample, along with selected magnifications of the regions highlighted by circles in (a) and (d) showing homojunctions (b and e) and the corresponding FFT of the images (c, f). Representative HRTEM image (g) of the ABR sample, along with a magnification (h) of the region highlighted by a circle in section (g), showing anatase/brookite heterojunction and the corresponding FFT of the image (i). The instrumental magnification was 500,000× (a, g) and 1000000× (d).

mode) and the 610–612 cm^{-1} peaks (A_{1g} mode), the weak features around 273 cm^{-1}, 320 cm^{-1} and 357 cm^{-1}(shoulder evidenced by arrow) as well as a peak around 826 cm^{-1} (weak B_{2g} mode) [57,60]. Fortunately, the 447 cm^{-1} peak (E_g mode, generally the most intense for rutile) is not overlapped by any intense features due to anatase or brookite, making it a good indicator of rutile's presence. In fact, the presence of weak Raman signals of rutile in triphasic samples with a low rutile percentage ($\leq$ 12 %) can make its identification more challenging, as reported by Balapure and Ganesan [7].

Moreover, the comparison of the ABR and AB curves reveals that the peak width decreases in the presence of rutile due to the higher calcination temperature used for ABR synthesis. As reported by Sarngan et al. [60], the crystallite size tends to increase at higher treatment temperature, and larger crystallites may correspond to narrower Raman peaks. This result agrees with the larger crystallite size measured by XRD and the HRTEM analysis. The Raman spectrum of a commercial Degussa P25 consisting of an anatase and rutile mixture (with an approximate anatase/rutile = 85/15 mass ratio) shows sharp peaks (**Figure S.2**). Conversely, the broadening of Raman peaks in the AB spectrum may indicate either a smaller crystallite size or a higher presence of defects at the interface, which are essential for charge transfer in semiconductors. This phenomenon is also attributed to changes in interatomic forces and local symmetry, indicating interfacial interactions between different phases in hetero- and homojunctions [60]. This Raman feature supports the previously discussed HRTEM results concerning the occurrence of numerous small anatase/brookite homojunctions.

3.1.2. Electrochemical and optical properties

Electrochemical impedance spectroscopy (EIS) was performed to investigate the electrochemical properties of AB and ABR samples, with a focus on internal resistances (Fig. 5). The Nyquist plots were fitted by applying the equivalent circuit model reported in the lower inset.

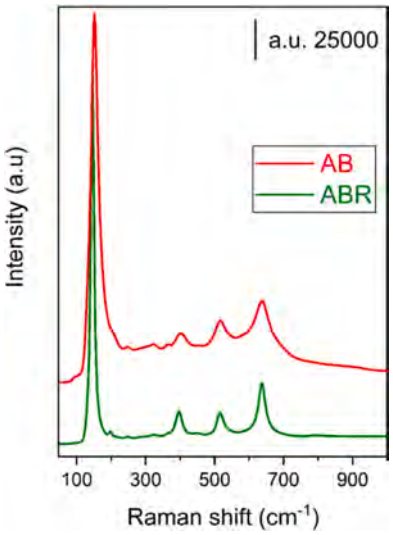

Fig. 4. Raman spectra of the AB (red curve) and ABR (green curve) samples.

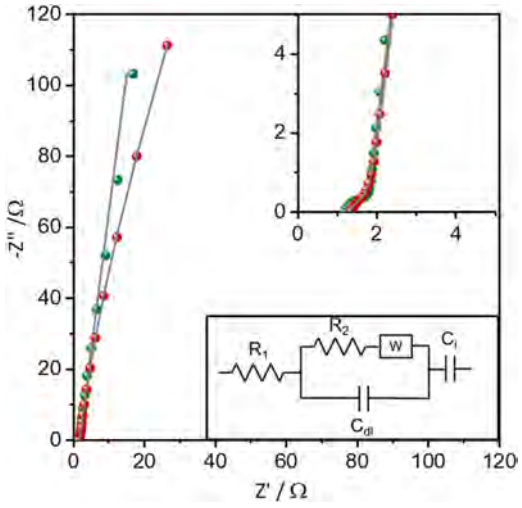

Fig. 5. Nyquist plots of TiO_2‖TiO_2 symmetric cell for both AB (red symbols) and ABR (green symbols) samples, along with the corresponding curve-fits (grey lines). The lower inset reports the equivalent circuit model used to curve-fit the Nyquist plots.

The Nyquist plots of AB and ABR samples are characterized by a very small semicircle at high frequencies and a linear trend at low frequencies. While the latter is associated with Warburg diffusion, the former arises from the combined contribution of double-layer capacitance (C_{dl}) and charge transfer resistance (R_2) [61]. In particular, a low internal resistance in TiO_2 samples is generally associated with an effective separation of photogenerated electron/hole pairs and, consequently, with an efficient photocatalytic activity [62]. Both AB and ABR samples display low R_2 values (0.96 and 1.21 Ω, respectively), significantly lower than the R_2 measured for commercial Degussa P25 (approximately 8.24 Ω, as shown in **Figure S.3**) in the same conditions.

The steady-state photoluminescence (PL) spectra of the AB and ABR films exhibit distinct emission features that reflect differences in their electronic structure and charge recombination dynamics (Fig. 6a). The AB and ABR samples display nearly identical emission profiles with maxima centered at 425 nm, suggesting comparable band structures and defect states. In contrast, the commercial Degussa P25 film shows a broader PL band (**Figure S.4**), slightly red-shifted to around 440 nm, indicating a wider distribution of radiative recombination centers and

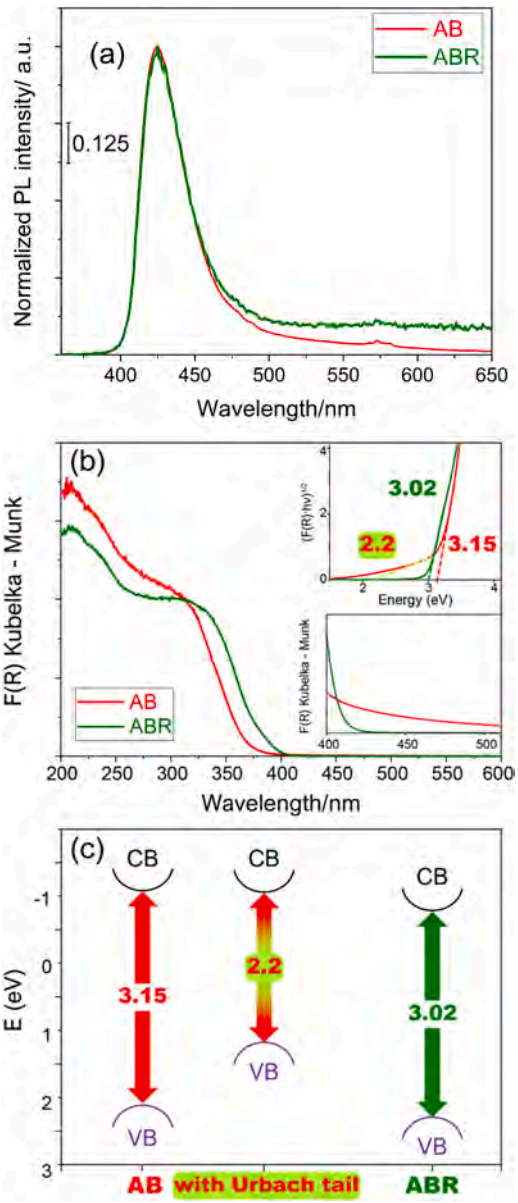

Fig. 6. (a) PL spectra of the AB anb ABR films; (b) DR UV Vis spectra of AB and ABR samples; lower inset: magnification of the spectra in the 400 – 525 nm range, highlighting the presence of an Urbach tail in the AB spectrum; upper inset: corresponding Tauc's plot for an indirect semiconductor model from which apparent E_{gap} values were extrapolated. (c) XPS-determined VB energy (eV) and CB energy values, which are calculated as CB = VB – E_{gap}.

possibly a higher contribution of surface or trap-mediated emission. The observed spectral broadening in Degussa P25 can be associated with the coexistence of anatase and rutile phases, which are known to create interfacial states that facilitate charge transfer and broaden the emission spectrum. The noisier PL signal observed for Degussa P25 arises from photobleaching under UV excitation, which required a reduction of the excitation bandwidth to minimize intensity decay during measurement. This behavior suggests that Degussa P25 is more susceptible to photo-induced structural or electronic changes, consistent with the known photocatalytic reactivity of mixed-phase TiO_2. Overall, the comparative PL analysis supports the hypothesis that AB and ABR homojunctions exhibit more efficient charge separation and fewer radiative recombination pathways than Degussa P25, which is consistent with their narrower and more stable emission responses. Unfortunately, the photoluminescence quantum yield (PLQY) of all the studied films (not

reported) was below the detection limit of the FLS1000 spectrofluorometer equipped with the QYPro™ integrating sphere, indicating an extremely weak radiative recombination efficiency. This behavior is consistent with previous reports on TiO_2-based materials, where the PLQY typically lies below 0.01 % due to the predominance of non-radiative recombination pathways [63,64] In TiO_2, photoexcited electrons and holes are efficiently trapped by lattice defects, surface states, or phase boundaries, leading to charge recombination through phonon emission rather than photon emission. The very low PLQY thus reflects the intrinsic nature of TiO_2 as a wide-bandgap semiconductor with a high density of defect-mediated non-radiative centers. From a photocatalytic perspective, this observation is favorable, as it implies that a significant fraction of photoexcited carriers participate in surface redox processes instead of recombining radiatively. The comparable absence of measurable PLQY in the studied TiO_2 samples suggests that the introduction of junction interfaces in AB and ABR does not significantly increase the radiative recombination probability, supporting the interpretation that these structures maintain efficient charge separation conducive to enhanced photocatalytic activity.

To investigate the influence of homojunctions on light absorption, the electronic properties of the AB and ABR powders are investigated using DR UV–Vis spectroscopy to determine the apparent band gap energy (E_{gap}, eV) and XPS to determine the Valence Band energy (VB, eV).

The DR UV–Vis spectra (Fig. 6b) exhibit the characteristic electronic transitions of undoped TiO_2, due to charge transfer from O^{2-} to Ti^{4+}. Tauc's plots (upper inset in Fig. 6b) are used to calculate the E_{gap} values for the samples, assuming an indirect semiconductor behaviour ($(F(R)*h\nu)^{1/2}$) as anatase is the predominant phase. The AB sample has an E_{gap} of 3.15 eV, while the ABR sample has a slightly lower E_{gap} of 3.02 eV. This difference is attributed to the presence of rutile in the ABR sample.

When the DR UV–Vis spectra are magnified in the 400–550 nm range (lower inset in Fig. 6b), the AB sample shows a tail extending towards longer wavelengths. This tail is not observed with the ABR sample. The AB sample's tail corresponds to a pronounced Urbach tail in the Tauc's plot (upper inset in Fig. 6b). An Urbach tail is an exponential part of a material's absorption coefficient spectrum that can appear near the optical band edge. Urbach tails can appear in amorphous, disordered, and crystalline materials, including undoped mixed TiO_2 phases [65]. The Urbach tail in the AB sample results in a significantly smaller E_{gap} value (approximately 2.2 eV, upper inset **in** Fig. 6b), which could allow the AB sample to absorb visible light in the light-green region, despite its larger band gap.

XPS analysis provides the VB energy values, which are used in combination with the E_{gap} values to determine the Conduction Band (CB) energy of the AB and ABR samples (Table 2 and Fig. 6c). It is worth noting that XPS directly measures the VB position, but the E_{gap} values are calculated assuming an indirect semiconductor model due to the abundance of anatase. However, the presence of anatase/brookite homojunctions could potentially alter the CB energy position. For completeness, in Fig. 6c, we also reported the calculated value of VB considering the Urbach tail in the AB sample. In the literature, the Urbach tail is attributed to localized electronic mid-gap states, which can originate from dopant elements (such as metals or nitrogen), point defects (like oxygen vacancies), or lattice disorder [67–71]. To investigate the nature of the Urbach tail in the AB sample, XPS and IR spectroscopy analyses were conducted on the sample surface (vide infra).

3.1.3. Surface properties

The XP survey spectra of the elemental surface composition of the two samples indicate that only O and Ti are present, in addition to adventitious carbon (Table 2). The High-Resolution (HR) XP Spectrum in the Ti 2p line region (**Figure S.5**) shows the typical spin-orbit splitting doublet of Ti $2p_{3/2}$ and Ti $2p_{1/2}$ species. The observed splitting in the Ti 2p lines is constant and equal to 5.7 eV (Table 2), confirming the presence of only Ti^{4+} species and excluding the presence of Ti^{3+} species. The O 1 s line shows lattice oxygen, OH^- species, and adsorbed water molecules (**Figure S.5** and Table 2). The calcined powders were re-exposed to air, allowing any oxygen vacancies or Ti^{3+} species to react with atmospheric oxygen. Therefore, the Urbach tail observed with the AB sample must originate from a different type of defect.

The nature of oxygen-related surface species is essential for TiO_2 photocatalytic activity [72]. According to Deiana et al. [72], surface hydroxyls may act as trapping sites for holes and electrons moving across the surface [73]. Moreover, the TiO_2 surface may also react with nearby CO_2 molecules, forming different C-containing species. To better understand these aspects, IR spectroscopy was employed to study the surfaces of the samples after outgassing the powders at 100 and 200 °C, i.e., at different degrees of hydration, while still avoiding any phase change in the AB sample (calcined at 200 °C).

Fig. 7 shows the IR spectra of the AB and ABR samples after outgassing at 100 °C (Fig. 7a) and 200 °C (Fig. 7b).

In the 3800–3000 cm^{-1} hydroxyl stretching range (light pink background), both samples outgassed at 100 °C exhibit bands envelops due to the presence of several types of OH species and a broad, intense absorption due to hydrogen bonding to adsorbed water molecules at lower wavenumbers (Fig. 7a). With the AB sample, it is possible to identify bands at 3733, 3675, and 3637 cm^{-1} along with an intense and broad absorption centered at approximately 3390 cm^{-1}. The two bands at higher wavenumbers can be ascribed to the stretching modes of different surface OH groups, namely terminal (3733 cm^{-1}) and bridged hydroxyls (3675 cm^{-1}), likely at the surface of anatase (the most abundant phase). The band at 3637 cm^{-1} is due to the stretching mode of OH groups of adsorbed water molecules: the corresponding bending mode is observed at approximately 1630 cm^{-1} as a shoulder of the IR bands due to adsorbed carbonates-like species (vide infra). The broad absorption centred at approximately 3390 cm^{-1} is due to extended hydrogen bonding between surface OH groups and adsorbed species, namely water molecules and formic acid that can form during calcination at 200 °C (vide infra), along with CO_2, likely due to the low-temperature treatment in the presence of residual molecules of isopropanol (both a synthesis product and the solvent) adsorbed at the surface of the washed powder. Indeed, according to the literature, the type of C-containing species on the TiO_2 surface is strongly dependent on the type of pretreatment [74].

The ABR sample shows the presence of similar bands due to same surface OH groups with bands at 3733, 3675 and 3637 cm^{-1}. In contrast, the signal due to OH groups engaged in H-bonding is less intense (due to the lower SSA of the sample) and blue-shifted, due to the absence of adsorbed formic acid (Fig. 7a).

Table 2
Band gap values (E_{gap}), as determined using Tauc's plot method for an indirect semiconductor model. XPS-determined VB values (eV), CB values (eV) calculated as CB = VB – E_{gap}. and XPS-determined binding energy values (BE, eV) of the Ti 2p and the O 1 s lines [66].

Sample	E_{gap} (eV)	VB (eV)	CB (eV)	Ti 2p BE (eV)	O/Ti ratio	O 1 s BE (eV)		
						O^{2-} lattice	OH^-	H_2O/organic
AB	3.15	2.59	−0.56	464.33 458.63	2.0	529.88	531.30	532.66
ABR	3.02	2.75	−0.27	464.29 458.59	2.0	529.84	530.83	532.04

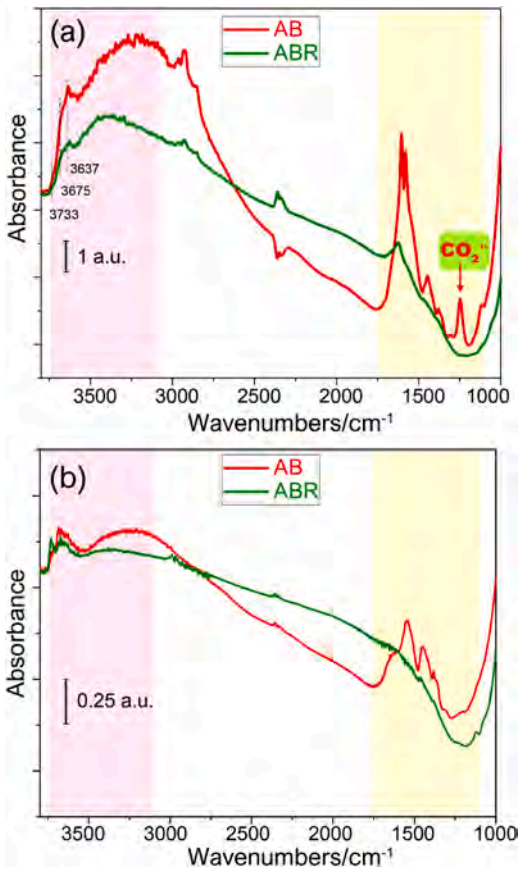

Fig. 7. IR spectra recorded on the AB and ABR samples after outgassing at 100 °C (a) and 200 °C (b). In both panels, the light pink background highlights the 3800–3000 cm^{-1} hydroxyl stretching range, and the light yellow background highlights the 1750–1100 cm^{-1} range where the bands of carbonates, bicarbonates, and formate species that may form on the surface of TiO_2 polymorphs occur.

CO_2 molecules can interact with the surface of different oxides, both in the dark and under illumination, forming several types of carbonates, carboxylates and also $CO_2^{\cdot-}$ that can be detected by IR spectroscopy [75–77]. The different types of carbonates, bicarbonates, and formate species that may form on the surface of TiO_2 polymorphs are all characterized by bands in the 1750–1100 cm^{-1} range (light yellow background) [74,78–83].

The ABR sample after outgassing at 100 °C (Fig. 7a) does not show the presence of C-containing species, which were likely decomposed during calcination at 600 °C. It only exhibits a band at 1624 cm^{-1}, readily ascribed to the bending mode of adsorbed water molecules (vide supra) [83]. On the contrary, the AB sample distinctly shows the IR bands of various C-containing species, namely formic acid molecules strongly perturbed by the interaction with the surface with characteristic bands at 1604 cm^{-1} (ν(C=O)) and 1307 cm^{-1} (ν(C—O)), formate ions (bands at 1545 and 1355 cm^{-1}) [84,85], bidentate carbonates (bands at 1580 and 1355 cm^{-1}), and monodentate carbonates (bands at 1445 and 1381 cm^{-1}) [80].

Interestingly, the additional band at 1250 cm^{-1} (red arrow) can be assigned to $CO_2^{\cdot-}$ radical ions, which are highly reactive intermediates in the reduction of CO_2, as discussed below [80]. As reported in the literature [86], CO_2 molecules can also adsorb on defective Ti^{3+} sites occurring on partially reduced TiO_2 without illumination, giving rise to bent $CO_2^{\cdot-}$ species characterized by IR features in the same range (vide infra).

In the OH stretching region (3800–3000 cm^{-1}), the AB sample dehydrated at 200 °C shows a band at 3730 cm^{-1}, a structured band with at least two contributions at 3665 and 3635 cm^{-1}, and a broad absorption centred at approximately 3240 cm^{-1} (Fig. 7b). As for the sample outgassed at 100 °C (Fig. 7a), the bands at 3730 and 3665 cm^{-1} can be attributed to terminal and bridging hydroxyls on anatase [87], although, according to the literature, OH groups of brookite could contribute to the band at 3730 cm^{-1} [88]. The bending mode of adsorbed water molecules is seen at 1640 cm^{-1}. The broad absorption centred at ca. 3240 cm^{-1} is due to H-bonded hydroxyls, redshifted likely by the interaction with (basic) formate species (vide infra). The ABR sample also shows the 3730 cm^{-1} band (which is slightly more intense than in AB) and the band at ca. 3665 cm^{-1}. In contrast, the band due to mutually interacting OH species is less intense and blue-shifted to 3400 cm^{-1} compared to AB, indicating that these are likely inter-particle OH groups, as evidenced by the absence of formate species.

In the 1700 −1100 cm^{-1} range, no bands ascribable to C-containing species are observed on the surface of the ABR sample outgassed at 200 °C (Fig. 7b). On the contrary, the AB sample outgassed at 200 °C shows bands due to adsorbed water molecules (1649 cm^{-1}), residual formate species (1545 and 1365 cm^{-1}), and monodentate carbonates (1450 and 1365 cm^{-1}). The band at 1250 cm^{-1} is no longer observed, indicating that $CO_2^{\cdot-}$ species are removed by outgassing at 200 °C.

Another essential feature is the surface charge, which can affect photocatalytic performance and is analyzed by measuring the ζ-potential curves, as shown in Fig. 8.

The TiO_2 surface is known to be amphoteric, as the Ti—OH surface groups can be protonated and deprotonated depending on pH. The pH at which the surface charge is neutral is referred to as the isoelectric point (pH_{IEP}). The samples have similar ζ-potential curves, with a pH_{IEP} between 2.4 and 2.8. This value is lower than that of other TiO_2 powders [89]. According to ref [90], the primary particle size and surface area, rather than the crystalline phase, influence the surface charge of TiO_2 nanoparticles synthesized by sol-gel methods. However, another study on hydrothermally treated samples found different pH_{IEP} values for brookite, anatase, and rutile samples, with brookite exhibiting the lowest pH_{IEP} and the strongest Brønsted acid sites. Additionally, they observed a slightly lower pH_{IEP} for samples with higher crystallinity [88]. The slightly lower pH_{IEP} of the ABR sample compared to AB can be attributed to its higher crystallinity (vide supra). Formic acid molecules at the surface of the AB sample could contribute to its lower pH_{IEP}, whereas they cannot contribute to the low value of the ABR sample, on which such species are absent. Therefore, the low pH_{IEP} of the AB and ABR samples may be primarily due to brookite-rich patches on the nanoparticle surfaces, possibly associated with the anatase/brookite homojunctions.

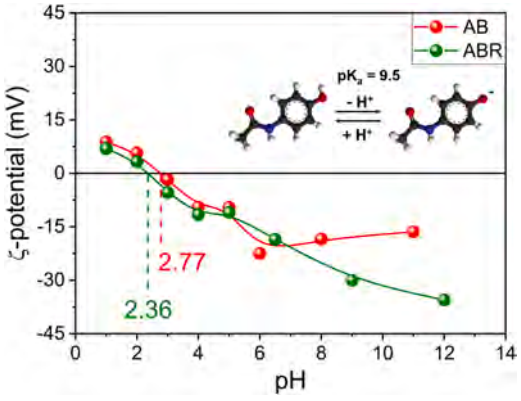

Fig. 8. ζ-potential curves of the AB and ABR samples at varying pH values. The inset reports the structure and protonation equilibrium of paracetamol (pK_a = 9.5).

3.2. Photocatalytic degradation of paracetamol under simulated solar light

The starting paracetamol solution used during the tests has a pH = 5.7; at this pH, the paracetamol molecule is neutral, and the surfaces of the AB and ABR samples are negatively charged (Fig. 8). Before photocatalytic tests, the powders were left for 1 h equilibrating with the paracetamol solution in dark conditions (spectra not shown): no relevant adsorption phenomena were observed, in agreement with the literature [91], indicating that the paracetamol molecules were not interacting strongly with the samples' surfaces in the adopted experimental conditions.

Since detailed analyses of the by-products and reaction pathways using conventional analytical techniques (e.g., HPLC-MS) are already well-established in the literature [45,46] we employed UV–vis spectroscopy and SERS investigation as powerful complementary tools to detect specific intermediates and support the proposed degradation mechanism.

The UV–Vis spectra obtained with a concentration of 0.15 g L^{-1} of the AB and ABR samples are shown in Fig. 9a and 9b, respectively.

The UV–Vis spectrum of the starting paracetamol solution shows two bands at 194 nm and 243 nm. The band at 194 nm is assigned to the π→π* electronic transition of the aromatic ring. The band at 243 nm is assigned to the n →π* electronic transition of the C=O group [45]. As reported in the literature [45], the percentage of paracetamol degradation is evaluated by measuring the intensity of the band at 243 nm in the UV–Vis spectra of supernatant aliquots that were withdrawn and analyzed at regular time intervals.

The insets to Fig. 9a and 9b report the C/C_0 trends over time derived from the absorbance intensity at 243 nm, in the presence of 0.15 g L^{-1} of AB (a) and ABR (b). We observe zero-order kinetics for the degradation of paracetamol in both samples. This observation aligns with the lack of paracetamol adsorption in dark conditions. Although pseudo-first-order kinetics can be observed for the photodegradation of paracetamol in the literature, most studies are conducted under different conditions (e.g., UV illumination, varying starting pH, and bubbling $O_{2(g)}$). Therefore, a direct comparison of the data is challenging [45,91]. As reported in ref [92], the apparent order of reaction may vary between 0 and 2, and zero-order kinetics is compatible with a limited oxygen supply, which is one of the possible reasons for the observed zero-order kinetics, as our system is not aerated. Indeed, with another set of TiO_2 powders, under the same conditions (illumination, photoreactor, catalyst concentration, oxygen supply, etc.), we already observed pseudo-zero-order kinetics of paracetamol photocatalytic degradation [93].

The AB sample exhibits a kinetic constant of 1.6 × 10^{-3} mol L^{-1} min^{-1}, comparable to the value we previously measured with Degussa P25 (2.5 × 10^{-3} mol L^{-1} min^{-1}), a standard benchmark in photocatalytic studies, which we tested under identical experimental conditions within the same photocatalytic reactor [93]. Moreover, Figure S.6 allows comparison of the UV–Vis spectra obtained after 5 h with 1 g L^{-1} of Degussa P25 and of AB, confirming the overall comparabòe activity of the two powders. The ABR powder shows lower activity. The AB sample's performance under simulated solar light can be attributed to the presence of numerous anatase/brookite homojunctions, as observed in HRTEM measurements (Fig. 3).

Additionally, the high surface area of the AB sample compared to the ABR sample may also contribute to the AB sample's performance. These results suggest that anatase/brookite homojunctions may have a synergistic effect on the utilization of simulated solar light. A cooperative effect has been observed previously with undoped TiO_2 anatase/brookite mixed phases under UV illumination [94] and with doped TiO_2 anatase/brookite mixed phases under visible light [94,95]. However, this is the first time it has been observed in undoped TiO_2 under simulated solar light.

Another set of experiments was performed with a higher photocatalyst concentration of 1.0 g L^{-1} (Fig. 9c and 9d). Under these

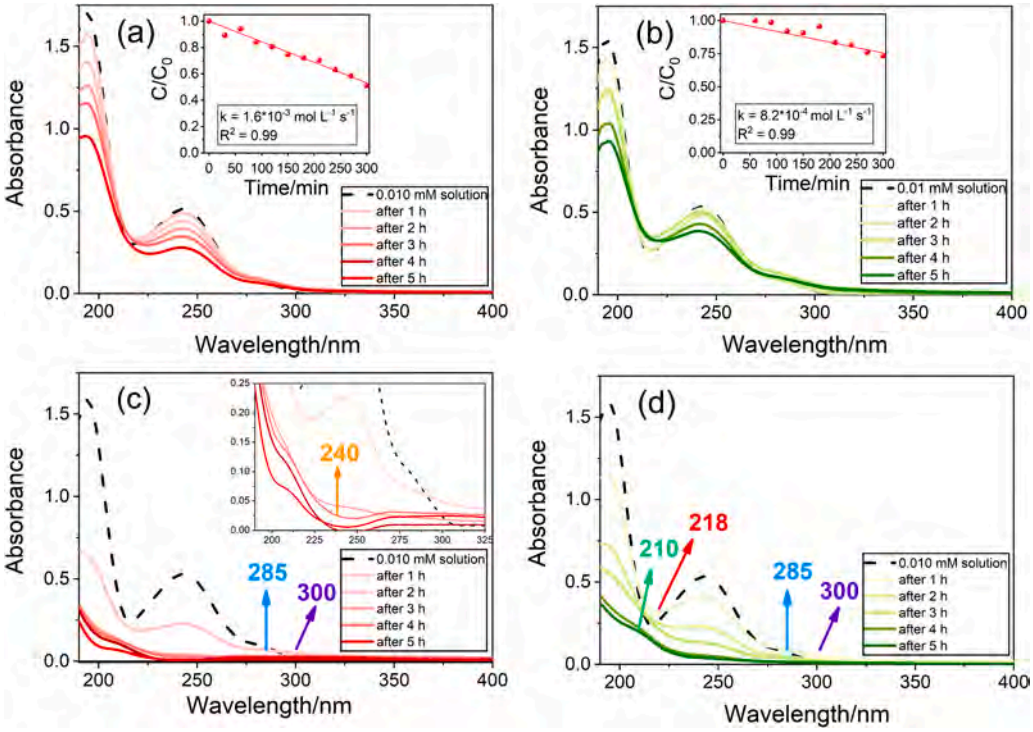

Fig. 9. UV–Vis spectra of the starting 0.01 mM paracetamol solution (dashed line) and of the supernatant aliquots withdrawn after 1, 2, 3, 4, and 5 h solar illumination with 0.15 g L^{-1} of AB (a) and ABR (b). Insets: corresponding degradation curves of paracetamol (C/C_0) as obtained by considering the intensity of the 243 nm band (circles) and linear curve fits obtained assuming zero-order kinetics. Panels (c) and (d) show UV–Vis spectra in the presence of 1.0 g L^{-1} of AB and ABR, respectively. Colored arrows indicate the bands ascribable to some possible by-products detailed in Scheme 2. Inset to Figure 9c highlights an inflection at 240 nm associated with intermediates such as HQ and 4-NP formed with degradation pathway "b" in Scheme 2.

conditions, the samples exhibit nearly complete degradation of paracetamol, with the bands at 194 nm and 243 nm of paracetamol almost absent after 5 h of irradiation. Various new absorbance bands appear during the experiment, indicating the formation of different by-products. These by-products are degraded at different rates depending on the photocatalyst used.

The two most common reaction pathways for paracetamol photocatalytic degradation, as described in the literature, are shown in Scheme 2 [45,46]. With both pathways, various aromatic by-products form during the photocatalytic degradation of paracetamol, but the final products are always small molecules, such as carboxylic acids.

The literature suggests that, primarily, the "b" pathway occurs [46]. Indeed, with Degussa P25 in the same experimental conditions, we previously observed a rapid decrease in paracetamol absorbance bands after 1 h of irradiation and the immediate formation of by-products through the "b" pathway in Scheme 2 [93].

Compared to the AB sample (Fig. 9c), which exhibits the fastest decrease in the main band at 243 nm after 1 h, the ABR sample (Fig. 9d) results in the complete degradation of paracetamol at a slower rate. This finding is in agreement with the slightly lower internal resistance calculated from the EIS measurement for AB with respect to ABR (Fig. 5).

The increased absorption at approximately 218 nm in the ABR sample's spectra (Fig. 9d) could be due to the formation of hydroxylated compounds (i.e., 1,2,4-trihydroxybenzene) after the loss of the $-NH-CO-CH_3$ group ("a" pathway in Scheme 2). These compounds are further photo-oxidized, forming carboxylic acids. The band at approximately 210 nm may be assigned to formic/acetic acids, which provides evidence for the formation of carboxylic acids, in agreement with Scheme 2 [45]. The UV–Vis spectra of the solutions obtained with AB and ABR samples did not show evidence of N-containing by-products, which could correspond to a less common degradation mechanism ("a" pathway in Scheme 2).

No absorbance bands ascribable to 4-AP are observed with the AB sample. However, a weak and broad absorption above 285 nm may indicate the presence of hydroquinone (HQ), which is found in both degradation pathways proposed in Scheme 2. An inflection point is observed at approximately 240 nm in the AB sample's spectrum taken after 3 h (inset to Fig. 9c). This peculiar spectral shape could be attributed to the presence of several possible by-products of paracetamol forming through the "b" pathway in Scheme 2, including HQ and 4-NP [96].

3.3. SERS assessment of the degradation pathway

After carefully inspecting the UV–Vis spectra and comparing them with literature data, to unravel the possible degradation pathway occurring with the AB sample (more promising than ABR in terms of photocatalytic activity), for both the tested catalyst concentrations of 0.15 and 1 g L^{-1} after 1 h of reaction in the presence of paracetamol (0.01 mM solution), we decided to use SERS to infer the nature of the products in the reaction solutions. Concerning the use of SERS for this aim, for instance, Au-based nanostructures have been employed for the detection of hydroquinone (HQ) [97] and paracetamol (PCT) [98]. Furthermore, the catalytic reduction of 4-nitrophenol (4-NP) to 4-aminophenol (4-AP) has been successfully monitored using "pomegranate"-like plasmonic nanoreactors with embedded Au nanoparticles [99]. Ag nanospheres decorating zinc oxide multi-pods have also demonstrated high efficiency in detecting 4-NP [51], whereas Ag nanoparticles have only been effectively employed for quantifying 4-AP in pharmaceutical formulations [100]. Notably, the Ag-decorated porous silicon/PDMS membranes developed by some of us stand out for their high-density distribution of plasmonic hot-spots, which enabled highly sensitive and versatile detection of analytes such as the Cyanine dyes (Cy3 and Cy5), Rhodamine 6 G [101,102], and microRNA biomarkers [103,104]. These characteristics make the platform a particularly robust and adaptable system for the aforementioned aim of detecting the reaction products in this work.

Fig. 10a and 10b report the Raman spectra of first spotted and then air-dried supernatants, alongside spectra obtained from solutions of pure reactants corresponding to PCT and its main possible degradation by-products (HQ, 4-AP, and 4-NP) mentioned in Scheme 2 (pathways "a" and "b") after deposition and air-drying on SERS substrates.

Assigning the highly overlapped Raman peaks to the vibrational features of the corresponding chemical species is a challenging task. Therefore, both the reactant powders and their 100 mM aqueous solutions (**Figure S.7**) were analysed under the same experimental conditions. High concentrations of the pure reactants can provide more intense and distinct Raman peaks in the collected spectra for comparison. Thus, a more straightforward interpretation of the Raman spectra of the supernatant residues may be advisable. Moreover, the absence of cross-interferences among functional chemical groups (sometimes the

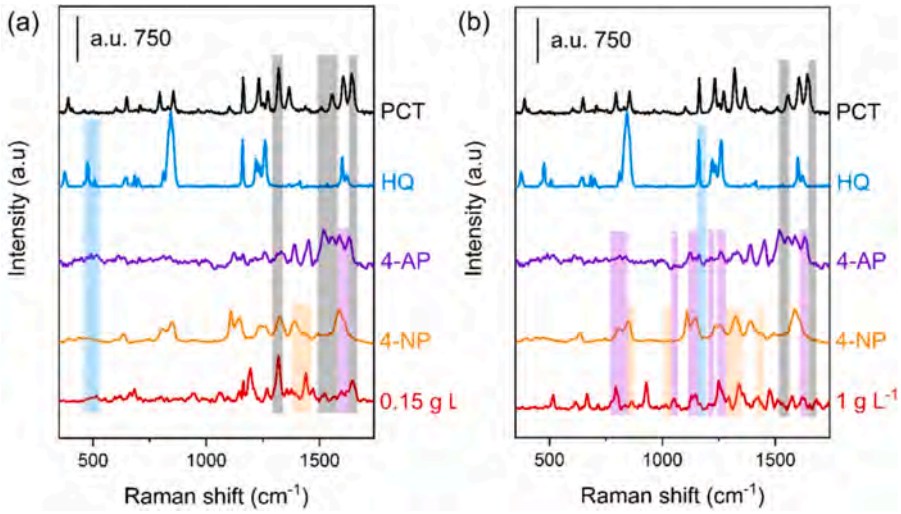

Fig. 10. Raman spectra on SERS substrate of the residue after spotting and left to air-dry a drop of the supernatant solution resulting after 1 h of reaction of the 0.01 mM paracetamol solution in the presence of 0.15 g L^{-1} (a) and 1 g L^{-1}(b) AB (red curves). Comparison is made with the Raman spectra of reference 100 mM solutions (spotted and air-dried drop) of hydroquinone (HQ, azure curve), 4-aminophenol (4-AP, violet curve), 4-nitrophenol (4-NP, orange curve), and paracetamol (PCT, black curve). Vertical stripes corresponding to the four reference molecules highlight the related assigned components in the red spectra (light grey: PCT; light violet: 4-AP; light orange: 4-NP, and azure: HQ).

same ones) belonging to different molecules under investigation can favour a distinct identification of features specific to each chemical species. Finally, this approach enables the assessment of the SERS substrate's influence on the scattering modes of these species, in terms of intensity and Raman shift positions, thereby facilitating the accurate identification of chemical species present in the supernatants.

Indeed, after thoroughly analyzing the literature data, it was possible to tentatively attribute the Raman features of the supernatant residue on the SERS substrate obtained after 1 h of paracetamol reaction in the presence of 1 g L^{-1} of AB (Fig. 10b). The spectrum shows at 380 cm^{-1} the γO + ring torsion, at 643 cm^{-1} the αO + CCC bending, and at 714 cm^{-1} the ring torsion, which are Raman modes observed for the α crystalline phase of HQ [105]. Additionally, Cabrera-Alonso reported a C=C very strong stretching mode at 1599–1620 cm^{-1} for SERS of HQ, assisted by gold nanorods, excited at 785 nm [97].

It is worth noting that SERS bands can be more intense than Raman bands, even shifted (typically 5–20 cm^{-1}) and the presence of additional peaks can be observed. In fact, the density of hot spots on the nanostructured metal substrate, where molecules adsorb, and their preferential orientation, while in contact with the surface, strongly influence the activation and enhancement of specific vibrational modes, complicating direct comparisons.

Other features are instead related to 4-AP (namely, peaks at 794 cm^{-1}, 838 cm^{-1}, 1050 cm^{-1}, 1128 cm^{-1}, 1145 cm^{-1} [106], 1206 cm^{-1}, 1248 cm^{-1}, 1620 cm^{-1} [99],) and to 4-NP (865–875 cm^{-1}, 1013 cm^{-1} [107], 1294 cm^{-1}, 1340 cm^{-1} [99], 1424 cm^{-1}) [107]. The peak centred between 1168 and 1178 cm^{-1} is assignable to the C—H in-plane bending of HQ [97], 4-AP [106], 4-NP [108] and, at the same time, to the phenyl-N bending in PCT [109]. This evidence suggests that, at this time of reaction (1 h), some unreacted paracetamol remains, in agreement with the UV–vis spectra in Fig. 9. Other paracetamol-related modes are observable at 1555–1559 cm^{-1} (amide II) and 1651 cm^{-1} (amide I) [110].

In the spectrum of supernatant residue on SERS substrate, obtained after 1 h of reaction in contact with 0.15 g L^{-1} of AB (Fig. 10a), the presence of unreacted paracetamol is more evident, maybe due to the presence of a lower amount of AB powder in the reaction batch, for the same (short) reaction time. For instance, here, the peak centered at 1321 cm^{-1}, assignable to amide III, is very intense [98], while the bands in the 1510–1525 cm^{-1} range [109], around 1557 cm^{-1} (amide II) and at 1651 cm^{-1} (amide I) [110] exhibit improved resolution. Anyway, some by-product species can be singled out: the band at 1596 cm^{-1}, for 4-AP [106], and the peaks in the 1340–1390 cm^{-1} range [99] and at 1437 cm^{-1}, for 4-NP [108]. The C=C aromatic ring stretching mode, centred at 1615 cm^{-1} and common to PCT [111], 4-AP [106] and 4-NP [99], is superimposed on the other signals. Finally, at low Raman shifts, the convolved band in the range 450–530 cm^{-1} can be distinctly assigned to HQ [112]. A detailed assignment of the observed Raman modes is reported in Tables 3 and 4 for experiments obtained in the presence of 0.15 g L^{-1} AB and 1.0 g L^{-1} AB, respectively.

Interestingly, the co-presence of Raman features coming from the main possible by-products of paracetamol photodegradation, already after 1 h of reaction time, suggests that the "b" pathway of Scheme 2 could be the most reliable one to propose. Moreover, the formation of radical species enables rapid interaction, yielding oxidation products (such as 4-NP and HQ), while PCT can be present in a partially unreacted state. The SERS investigation, therefore, shows that with the AB sample, the "b" pathway in Scheme 2 is very probable, as already observed with Degussa P25 [93] and in agreement with the similar apparent kinetic constants of the two TiO_2 powders. For a more accurate identification and quantification of the species resulting from paracetamol decomposition, future studies should incorporate multivariate analysis techniques, such as Principal Component Analysis (PCA), on a larger and statistically meaningful SERS dataset. Therefore, this study uniquely demonstrates the SERS-assisted identification of paracetamol degradation intermediates on anatase/brookite TiO_2.

3.4. On the formation of $CO_2^{\cdot-}$ species on the surface of the AB sample and their prospective role in photocatalysis

Besides the photocatalytic degradation of paracetamol under simulated solar light, the formation of $CO_2^{\cdot-}$ on the surface of the AB sample is relevant, as $CO_2^{\cdot-}$ species are widely recognized as the initial and crucial intermediates in CO_2 reduction processes, particularly for applications in solar fuel production. However, the direct generation of $CO_2^{\cdot-}$ from CO_2 remains challenging due to the molecule's high reduction potential.

Beyond its role in photocatalysis, $CO_2^{\cdot-}$ has recently attracted attention in organic synthesis as a versatile nucleophilic species and a powerful single-electron reductant, enabling the formation of valuable carboxylic acids. Typically, $CO_2^{\cdot-}$ is produced via direct electrochemical or photochemical reduction of CO_2, or through hydrogen atom transfer (HAT) from formate salts, especially in DMSO as a solvent [47]. Direct reduction of CO_2 may occur with strong reductants or by UV-irradiation. HAT with formate salts can occur under visible light.

The presence of $CO_2^{\cdot-}$ species in AB is likely due to the sample (calcined at 200 °C) having defects available for adsorbing CO_2 molecules or could derive from the HAT of adsorbed formate ions, also detected by IR spectroscopy (Fig. 7a). The ABR sample has a significantly lower SSA resulting from high-temperature calcination, which likely reduces or suppresses defects, potentially preventing the detection of surface $CO_2^{\cdot-}$ species by IR spectroscopy.

According to the literature, the formation of $CO_2^{\cdot-}$ on defective TiO_2

Table 3
Raman modes and assignments, coming from the analysis of the main presumed degradation by-products (HQ, 4-AP, and 4-NP), of the spectrum collected on SERS substrate of the residue after spotting and left to air-dry a drop of the supernatant solution resulting after 1 h of reaction in the presence of 0.15 g L^{-1} AB solution and paracetamol (0.01 mM).

Hydroquinone (HQ)		4-aminophenol (4-AP)		4-nitrophenol (4-NP)		Paracetamol (PCT)	
Raman shift (cm^{-1})	Assignment	Raman shift (cm^{-1})	Assignment	Raman shift (cm^{-1})	Assignment	Raman shift (cm^{-1})	Assignment
450–530	C-C-C planar deformation [112]						
				1340–1390	NO_2 symmetric stretching [99]	1321	amide III [98]
				1437	C—H in-plane bending [108]		
						1510–1525	*C=C* stretching/ N—H deformation [109]
		1596	In-plane N—H deformation and C–N stretch [106].			1555–1559	Amide II [110]
		1615	*C=C* aromatic ring stretch [106].	1615	*C=C* aromatic ring stretching [99]	1615	*C=C* aromatic ring stretching [111]
						1651	Amide I [110]

Table 4
Raman modes and assignments, coming from the analysis of the main presumed degradation by-products (HQ, 4-AP, and 4-NP), of the spectrum collected on SERS substrate of the residue after spotting and left to air-dry a drop of the supernatant solution resulting solution resulting after 1 h of reaction in the presence of 1.0 g L^{-1} AB solution and paracetamol (0.01 mM).

Hydroquinone (HQ)		4-aminophenol (4-AP)		4-nitrophenol (4-NP)		Paracetamol (PCT)	
Raman shift (cm^{-1})	Assignment	Raman shift (cm^{-1})	Assignment	Raman shift (cm^{-1})	Assignment	Raman shift (cm^{-1})	Assignment
380	γO + ring torsion [105]						
643	αO + CCC bending [105]						
714	Ring torsion [105]	794 [106]					
		838	Out-of-plane C—H bending [106]	865–875	NO_2 deformation [107]		
		1050	Ring breathing [106]	1013	C-H in-plane deformation [107]		
		1128	C—H bending [106]				
		1145	H-N-H bending [106]				
1168	C—H in-plane bending [97]	1170	C-H in-plane bending [106]	1168	C—H in-plane bending [108]	1168	Phenyl-N bending [109]
		1206 [99]					
		1248	C-H bending/C—NH_2 stretching [99]	1294 [99]			
				1340	NO_2 symmetric stretching [99]		
				1424	C—H in-plane deformation [107]		
1599–1620	*C*=*C* stretching (vs) [97]	1620	*C*=*C* stretching/ C—NH_2 stretching [99]			1555–1559	Amide II [110]
						1651	Amide I [110]

surfaces occurs when CO_2 molecules (produced during calcination at 200 °C) chemisorb onto Ti^{3+} sites through the following reaction [113, 114]:

$$Ti^{3+}_{(surf)} + CO_{2(gas)} \rightarrow Ti^{4+}_{(surf)} + CO^{-}_{2(surf)}$$

forming negatively charged bent species [86]. This process can also occur without illumination (as during the calcination procedure).

Different authors have reported that this process is favored in the presence of junctions in various types of nanomaterials [115,116]. Based on our results, the formation of $CO_2{\cdot}^-$ species is likely linked to surface defects in the AB sample. These defects are likely related to the anatase/brookite homojunctions observed by HRTEM and by Raman spectroscopy. With the same surface, the formation of adsorbed formate ions is observed, which could contribute to the formation of $CO_2{\cdot}^-$ species.

$CO_2{\cdot}^-$ species may play several vital roles. Being electron-withdrawing species, they lower the VB edge, which leads to a narrower band gap. Indeed, XPS analysis reveals that the AB sample exhibits a lower VB energy (Table 2), which can also be attributed to the presence of the $CO_2{\cdot}^-$ species. Lower VB energy values enhance the oxidation ability of photogenerated holes and expand the range of light to which the sample can respond. Therefore, $CO_2{\cdot}^-$ species can promote the separation of photogenerated charge carriers and also act as photosensitizers, allowing TiO_2 to absorb visible light and become photocatalytically active under visible light giving rise to the Urbach tail observed in the DR UV–Vis spectrum of the AB sample (lower inset in Fig. 6b), primarily due to the presence of more localized states within the band gap. The electron-withdrawing effect of the $CO_2{\cdot}^-$ species may also be responsible for the slightly higher binding energy of the Ti 2p line in the AB sample (Table 2).

We can infer that anatase/brookite homojunctions can be a straightforward method for generating $CO_2{\cdot}^-$ species under mild conditions in the presence of TiO_2, with the resulting radical species stabilized on its surface.

4. Conclusions

A high surface area anatase/brookite mixed phase (AB sample) was synthesized using a template-free sol-gel method based on pH control (pH = 2.00) followed by mild calcination at 200 °C. In this mixed phase, brookite is always associated with anatase, forming numerous and small anatase/brookite homojunctions that act as photocatalytically efficient defect sites, enhancing charge separation and facilitating rapid electron transfer.

Calcination at a higher temperature (600 °C) produces an anatase/brookite/rutile mixed phase, which still has anatase/brookite homojunctions, but also a lower specific surface area and higher charge transfer resistance, thus making the photocatalyst less active in terms of reaction rate, yet still capable of reaching complete paracetamol conversion in the adopted reaction conditions.

Surface-enhanced Raman scattering confirms that the degradation of paracetamol in the presence of anatase/brookite mixed phase likely occurs through a degradation pathway already observed with TiO_2. While this pathway has already been reported in the literature using more resource-intensive techniques, our findings demonstrate that SERS provides a powerful and less demanding experimental technique for intermediates detection, highlighting the synergy between the structural design of the photocatalyst and the analytical resolution of the reaction products.

The anatase/brookite mixed phase also promotes the formation of CO_2^- radical ions, which are recognized as the starting point of the CO_2 reduction process and also valuable species in organic synthesis, suggesting that anatase/brookite homojunctions in TiO_2 can promote its formation under mild conditions, inferring additional functionality of these defects for synthetic applications. The dual capability of anatase/brookite homojunctions, which can either remove emerging pollutants or produce chemically valuable radical intermediates, broadens the functional horizon of mixed-phase photocatalysts.

Funding sources

This study was carried out within the «GREEN UP: GREENER NANOMATERIALS FOR UPCONVERSION IN PHOTOCATALYTIC APPLICATIONS» project –funded by the Ministero dell'Università e della Ricerca –within the PRIN 2022 program (D.D.104 –02/02/2022) funded by the European Union - Next Generation EU. This manuscript

reflects only the authors' views and opinions and the Ministry cannot be considered responsible for them".

F.S.F. acknowledges the LuSH Art project "Luminescent Solar Heterostructures for Artificial photosynthesis" (Marie Curie Action, European Union Horizon 2020 research and innovation program, grant agreement no 843439) for the initial part of this work.

A.P. acknowledges the Italian Ministry for University and Research (MUR) for funding under the D.M. 1062/2021 program.

H.D. acknowledges the Italian Ministry for University and Research (MUR) for funding under the National Recovery and Resilience Plan (PNRR Mission 4, Component 2, Investment 1.3 – D.D. 1561 11.10.2022 of the Ministero dell'Università e della Ricerca (MUR), PE0000021), within the NEST – Network 4 Energy Sustainable Transition. This manuscript reflects only the authors' views and opinions, neither the European Union nor the European Commission can be considered responsible for them.

N.B., F.S.F., P.R., A.P., H.D. and B.B acknowledge support under the MUR program "Dipartimenti di Eccellenza 2023–2027″ (CUPE17G22001490006).

CRediT authorship contribution statement

Nicola Blangetti: Writing – original draft, Investigation, Formal analysis. **Francesca S. Freyria:** Writing – review & editing, Visualization, Investigation, Funding acquisition, Conceptualization. **Maela Manzoli:** Writing – original draft, Visualization, Investigation, Formal analysis. **Paola Rivolo:** Writing – original draft, Visualization, Investigation, Formal analysis. **Alessandro Piovano:** Writing – original draft, Visualization, Investigation, Formal analysis. **Hamideh Darjazi:** Writing – original draft, Visualization, Investigation, Formal analysis. **Nicoletta Ditaranto:** Writing – original draft, Investigation, Formal analysis. **Barbara Patrizi:** Formal analysis, Investigation, Writing – review & editing. **Sandra Doria:** Formal analysis, Investigation, Writing – review & editing. **Barbara Bonelli:** Writing – review & editing, Writing – original draft, Visualization, Supervision, Resources, Project administration, Methodology, Conceptualization.

Declaration of competing interest

The authors declare that they have no known competing financial interests or personal relationships that could have appeared to influence the work reported in this paper.

Acknowledgments

The authors thank Prof. S. Hernández (from the Department of Applied Science and Technology at Politecnico di Torino) for lending the simulated solar spectrum lamp, Prof. T. Tosco (from the Department of Environment, Land and Infrastructure Engineering at Politecnico di Torino, Italy) for lending the DLS instrument and Dr Gianluigi Marra (Istituto Eni Donegani Eni Sp.a. Renewable, New Energies and Material Science Research Center (DE-R&D)) for his support on the Rietveld refinement.

Supplementary materials

Supplementary material associated with this article can be found, in the online version, at doi:10.1016/j.apsadv.2025.100896.

Data availability

Data will be made available on request.

References

[1] M. Manzoli, F.S. Freyria, N. Blangetti, B. Bonelli, Brookite, a sometimes under evaluated TiO_2 polymorph, RSC. Adv. 12 (2022) 3322–3334, https://doi.org/10.1039/d1ra09057g.

[2] S.-Y. Lee, S.-J. Park, TiO_2 photocatalyst for water treatment applications, J. Ind. Eng. Chem. 19 (2013) 1761–1769, https://doi.org/10.1016/j.jiec.2013.07.012.

[3] A. Majumder, D. Saidulu, A.K. Gupta, P.S. Ghosal, Predicting the trend and utility of different photocatalysts for degradation of pharmaceutically active compounds: a special emphasis on photocatalytic materials, modifications, and performance comparison, J. Environ. Manage. 293 (2021) 112858, https://doi.org/10.1016/J.JENVMAN.2021.112858.

[4] K. Prakruthi, M.P. Ujwal, S.R. Yashas, B. Mahesh, N. Kumara Swamy, H. P. Shivaraju, Recent advances in photocatalytic remediation of emerging organic pollutants using semiconducting metal oxides: an overview, Environ. Sci. Pollut. Res. 29 (2021) 4930–4957, https://doi.org/10.1007/S11356-021-17361-1, 2021 29:4.

[5] J. Buckeridge, K.T. Butler, C.R.A. Catlow, A.J. Logsdail, D.O. Scanlon, S. A. Shevlin, S.M. Woodley, A.A. Sokol, A. Walsh, Polymorph engineering of TiO_2: demonstrating how absolute reference potentials are determined by local coordination, Chem. Mater. 27 (2015) 3844–3851, https://doi.org/10.1021/acs.chemmater.5b00230.

[6] S. Cao, N. Sui, P. Zhang, T. Zhou, J. Tu, T. Zhang, TiO_2 nanostructures with different crystal phases for sensitive acetone gas sensors, J. Colloid. Interface Sci. 607 (2022) 357–366, https://doi.org/10.1016/j.jcis.2021.08.215.

[7] A. Balapure, R. Ganesan, Anatase versus Triphasic TiO_2: near-identical synthesis and comparative structure-sensitive photocatalytic degradation of methylene blue and 4-chlorophenol, J. Colloid. Interface Sci. 581 (2021) 205–217, https://doi.org/10.1016/j.jcis.2020.07.096.

[8] G. Žerjav, K. Žižek, J. Zavašnik, A. Pintar, Brookite vs. rutile vs. anatase: what's behind their various photocatalytic activities? J. Environ. Chem. Eng. 10 (2022) 107722 https://doi.org/10.1016/j.jece.2022.107722.

[9] M.G. Kim, J.E. Lee, K.S. Kim, J.M. Kang, J.H. Lee, K.H. Kim, M. Cho, S.G. Lee, Photocatalytic degradation of methylene blue under UV and visible light by brookite-rutile bi-crystalline phase of TiO_2, New J. Chem. 45 (2021) 3485–3497, https://doi.org/10.1039/d0nj05162d.

[10] T.S. Atabaev, A. Molkenova, Upconversion optical nanomaterials applied for photocatalysis and photovoltaics: recent advances and perspectives, Front. Mater. Sci. 13 (2019) 335–341, https://doi.org/10.1007/s11706-019-0482-z.

[11] K. Ozawa, M. Emori, S. Yamamoto, R. Yukawa, S. Yamamoto, R. Hobara, K. Fujikawa, H. Sakama, I. Matsuda, Electron-hole recombination time at TiO_2 single-crystal surfaces: influence of surface band bending, J. Phys. Chem. Lett. 5 (2014) 1953–1957, https://doi.org/10.1021/jz500770c.

[12] W. Srevarit, S. Moonmangmee, P. Phapugrangkul, S. Kuboon, A. Klamchuen, N. Saito, C. Ponchio, Photoelectrocatalytic H_2 evolution enhancement over CuO-decorated TiO_2 nanocatalysts and promoting *E. coli* degradation, J. Alloys. Compd. 859 (2021), https://doi.org/10.1016/j.jallcom.2020.157818.

[13] S.G. Ullattil, S.B. Narendranath, S.C. Pillai, P. Periyat, Black TiO_2 nanomaterials: a review of recent advances, Chem. Eng. J. 343 (2018) 708–736, https://doi.org/10.1016/J.CEJ.2018.01.069.

[14] L. Wang, J. Yu, Principles of photocatalysis. Interface Science and Technology, Elsevier B.V., 2023, pp. 1–52, https://doi.org/10.1016/B978-0-443-18786-5.00002-0.

[15] G. Li, K.A. Gray, The solid-solid interface: explaining the high and unique photocatalytic reactivity of TiO_2-based nanocomposite materials, Chem. Phys. 339 (2007) 173–187, https://doi.org/10.1016/j.chemphys.2007.05.023.

[16] J. Moma, J. Baloyi, Modified titanium dioxide for photocatalytic applications. Photocatalysts - Applications and Attributes, IntechOpen, 2018, https://doi.org/10.5772/intechopen.79374.

[17] M. Piumetti, F.S. Freyria, M. Armandi, F. Geobaldo, E. Garrone, B. Bonelli, Fe- and V-doped mesoporous titania prepared by direct synthesis: characterization and role in the oxidation of AO7 by H_2O_2 in the dark, Catal. Today 227 (2014), https://doi.org/10.1016/j.cattod.2013.11.013.

[18] F.S. Freyria, M. Compagnoni, N. Ditaranto, I. Rossetti, M. Piumetti, G. Ramis, B. Bonelli, Pure and Fe-doped mesoporous titania catalyse the oxidation of acid orange 7 by H_2O_2 under different illumination conditions: fe doping improves photocatalytic activity under simulated solar light, Catalysts. 7 (2017), https://doi.org/10.3390/catal7070213.

[19] L. Zeng, Z. Lu, M. Li, J. Yang, W. Song, D. Zeng, C. Xie, A modular calcination method to prepare modified N-doped TiO_2 nanoparticle with high photocatalytic activity, Appl. Catal. B 183 (2016) 308–316, https://doi.org/10.1016/J.APCATB.2015.10.048.

[20] J. Chen, M. Guan, X. Zhang, X. Gong, Insights into a rutile/brookite homojunction of titanium dioxide: separated reactive sites and boosted photocatalytic activity, RSC. Adv. 9 (2019) 36615–36620, https://doi.org/10.1039/c9ra07483j.

[21] X. Ruan, X. Cui, Y. Cui, X. Fan, Z. Li, T. Xie, K. Ba, G. Jia, H. Zhang, L. Zhang, W. Zhang, X. Zhao, J. Leng, S. Jin, D.J. Singh, W. Zheng, Favorable energy band alignment of TiO_2 anatase/rutile heterophase homojunctions yields photocatalytic hydrogen evolution with quantum efficiency exceeding 45.6%, Adv. Energy Mater. 12 (2022) https://doi.org/10.1002/aenm.202200298.

[22] X. Jiang, M. Manawan, T. Feng, R. Qian, T. Zhao, G. Zhou, F. Kong, Q. Wang, S. Dai, J.H. Pan, Anatase and rutile in evonik aeroxide P25: heterojunctioned or individual nanoparticles? Catal. Today 300 (2018) 12–17, https://doi.org/10.1016/j.cattod.2017.06.010.

[23] T. Ohno, K. Sarukawa, K. Tokieda, M. Matsumura, Morphology of a TiO_2 photocatalyst (Degussa, P-25) consisting of anatase and rutile crystalline phases, J. Catal. 203 (2001) 82–86, https://doi.org/10.1006/JCAT.2001.3316.

[24] T. Ohno, K. Tokieda, S. Higashida, M. Matsumura, Synergism between rutile and anatase TiO_2 particles in photocatalytic oxidation of naphthalene, Appl. Catal. A Gen. 244 (2003) 383–391, https://doi.org/10.1016/S0926-860X(02)00610-5.

[25] C. Wu, Y. Yue, X. Deng, W. Hua, Z. Gao, Investigation on the synergetic effect between anatase and rutile nanoparticles in gas-phase photocatalytic oxidations, Catal. Today 93–95 (2004) 863–869, https://doi.org/10.1016/j.cattod.2004.06.087.

[26] B.X. Zhou, S.S. Ding, Y. Wang, X.R. Wang, W.Q. Huang, K. Li, G.F. Huang, Type-II/type-II band alignment to boost spatial charge separation: a case study of g-C_3N_4 quantum dots/a-TiO_2/r-TiO_2 for highly efficient photocatalytic hydrogen and oxygen evolution, Nanoscale 12 (2020) 6037–6046, https://doi.org/10.1039/D0NR00176G.

[27] D.C. Hurum, A.G. Agrios, K.A. Gray, T. Rajh, M.C. Thurnauer, Explaining the enhanced photocatalytic activity of Degussa P25 mixed-phase TiO_2 using EPR, J. Phys. Chem. B 107 (2003) 4545–4549, https://doi.org/10.1021/JP0273934/ASSET/IMAGES/LARGE/JP0273934F00005.JPEG.

[28] S. Shen, X. Wang, T. Chen, Z. Feng, C. Li, Transfer of photoinduced electrons in anatase-rutile TiO_2 determined by time-resolved mid-infrared spectroscopy, J. Phys. Chem. C 118 (2014) 12661–12668, https://doi.org/10.1021/jp502912u.

[29] D. Salazar-Marín, G. Oza, J.A.D. Real, A. Cervantes-Uribe, H. Pérez-Vidal, M. K. Kesarla, J.G.T. Torres, S. Godavarthi, Distinguishing between type II and S-scheme heterojunction materials: a comprehensive review, Appl. Surf. Sci. Adv. 19 (2024), https://doi.org/10.1016/j.apsadv.2023.100536.

[30] C. Nie, X. Wang, P. Lu, Y. Zhu, X. Li, H. Tang, Advancements in S-scheme heterojunction materials for photocatalytic environmental remediation, J. Mater. Sci. Technol. 169 (2024) 182–198, https://doi.org/10.1016/j.jmst.2023.06.011.

[31] Q. Tay, X. Wang, X. Zhao, J. Hong, Q. Zhang, R. Xu, Z. Chen, Enhanced visible light hydrogen production via a multiple heterojunction structure with defect-engineered g-C_3N_4 and two-phase anatase/brookite TiO_2, J. Catal. 342 (2016) 55–62, https://doi.org/10.1016/j.jcat.2016.07.007.

[32] S. Gervasi, N. Blangetti, F.S. Freyria, S. Guastella, B. Bonelli, Undoped and Fe-doped anatase/brookite TiO_2 mixed phases, obtained by a simple template-free synthesis method: physico-chemical characterization and photocatalytic activity towards simazine degradation, Catalysts. 13 (2023) 667, https://doi.org/10.3390/catal13040667, n°.

[33] F.S. Freyria, N. Blangetti, S. Esposito, R. Nasi, M. Armandi, V. Annelio, B. Bonelli, Effects of the Brookite phase on the properties of different nanostructured TiO_2 phases photocatalytically active towards the degradation of N-phenylurea, ChemistryOpen. 9 (2020) 903–912, https://doi.org/10.1002/open.202000127.

[34] S.M. El-Sheikh, T.M. Khedr, A.A. Ismial, W.A. Badawy, Efficient mesoporous anatase-brookiteTiO2 photocatalysts for degradation of ibuprofen, in: n.d.

[35] V. Etacheri, G. Michlits, M.K. Seery, S.J. Hinder, S.C. Pillai, A highly efficient $TiO_{2-x}C_x$ nano-heterojunction photocatalyst for visible light induced antibacterial applications, ACS. Appl. Mater. Interfaces. 5 (2013) 1663–1672, https://doi.org/10.1021/am302676a.

[36] M. Patel, R. Kumar, K. Kishor, T. Mlsna, C.U. Pittman, D. Mohan, Pharmaceuticals of emerging concern in aquatic systems: chemistry, occurrence, effects, and removal methods, Chem. Rev. 119 (2019) 3510–3673, https://doi.org/10.1021/acs.chemrev.8b00299.

[37] O.F.S. Khasawneh, P. Palaniandy, Occurrence and removal of pharmaceuticals in wastewater treatment plants, Process Saf. Environ. Prot. 150 (2021) 532–556, https://doi.org/10.1016/j.psep.2021.04.045.

[38] G.R. Boyd, H. Reemtsma, D.A. Grimm, S. Mitra, Pharmaceuticals and personal care products (PPCPs) in surface and treated waters of Louisiana, USA and Ontario, Canada, Sci. Total Environ. 311 (2003) 135–149, https://doi.org/10.1016/S0048-9697(03)00138-4.

[39] A.O. Oluwole, E.O. Omotola, O.S. Olatunji, Pharmaceuticals and personal care products in water and wastewater: a review of treatment processes and use of photocatalyst immobilized on functionalized carbon in AOP degradation, BMC. Chem. 14 (2020) 1–29, https://doi.org/10.1186/s13065-020-00714-1.

[40] J.L. Wilkinson, A.B.A. Boxall, D.W. Kolpin, K.M.Y. Leung, R.W.S. Lai, C. Galban-Malag, A.D. Adell, J. Mondon, M. Metian, R.A. Marchant, A. Bouzas-Monroy, A. Cuni-Sanchez, A. Coors, P. Carriquiriborde, M. Rojo, C. Gordon, M. Cara, M. Moermond, T. Luarte, V. Petrosyan, Y. Perikhanyan, C.S. Mahon, C.J. McGurk, T. Hofmann, T. Kormoker, V. Iniguez, J. Guzman-Otazo, J.L. Tavares, F.G. de Figueiredo, M.T.P. Razzolini, V. Dougnon, G. Gbaguidi, O. Traore, J.M. Blais, L. E. Kimpe, M. Wong, D. Wong, R. Ntchantcho, J. Pizarro, G.G. Ying, C.E. Chen, M. Paez, J. Martınez-Lara, J.P. Otamonga, J. Pote, S.A. Ifo, P. Wilson, S. Echeverrıa-Saenz, N. Udikovic-Kolic, M. Milakovic, D. Fatta-Kassinos, L. Ioannou-Ttofa, V. Belusova, J. Vymazal, M. Cardenas-Bustamante, B.A. Kassa, J. Garric, A. Chaumot, P. Gibba, I. Kunchulia, S. Seidensticker, G. Lyberatos, H. P. Halldorsson, M. Melling, T. Shashidhar, M. Lamba, A. Nastiti, A. Supriatin, N. Pourang, A. Abedini, O. Abdullah, S.S. Gharbia, F. Pilla, B. Chefetz, T. Topaz, K.M. Yao, B. Aubakirova, R. Beisenova, L. Olaka, J.K. Mulu, P. Chatanga, V. Ntuli, N.T. Blama, S. Sherif, A.Z. Aris, L.J. Looi, M. Niang, S.T. Traore, R. Oldenkamp, O. Ogunbanwo, M. Ashfaq, M. Iqbal, Z. Abdeen, A. O'Dea, J.M. Morales-Saldaña, M. Custodio, H. de la Cruz, I. Navarrete, F. Carvalho, A.B. Gogra, B.M. Koroma, V. Cerkvenik-Flajs, M. Gombac, M. Thwala, K. Choi, H. Kang, J.L. Celestino Ladu, A. Rico, P. Amerasinghe, A. Sobek, G. Horlitz, A.K. Zenker, A.C. King, J.J. Jiang, R. Kariuki, M. Tumbo, U. Tezel, T.T. Onay, J.B. Lejju, Y. Vystavna, Y. Vergeles, H. Heinzen, A. Perez-Parada, D.B. Sims, M. Figy, D. Good, C. Teta, Pharmaceutical pollution of the world's rivers, Proc. Natl. Acad. Sci. USA 119 (2022), https://doi.org/10.1073/PNAS.2113947119/SUPPL_FILE/PNAS.2113947119.SD12.XLSX.

[41] K.O. Badmus, J.O. Tijani, E. Massima, L. Petrik, Treatment of persistent organic pollutants in wastewater using hydrodynamic cavitation in synergy with advanced oxidation process, Environ. Sci. Pollut. Res. 25 (2018) 7299–7314, https://doi.org/10.1007/s11356-017-1171-z.

[42] X. Wei, Q. Zhang, S. Cao, X. Xu, Y. Chen, L. Liu, R. Yang, J. Chen, B. Lv, Removal of pharmaceuticals and personal care products (PPCPs) and environmental estrogens (EEs) from water using positively charged hollow fiber nanofiltration membrane, Environ. Sci. Pollut. Res. 28 (2021) 8486–8497, https://doi.org/10.1007/s11356-020-11103-5.

[43] F.S. Freyria, F. Geobaldo, B. Bonelli, Nanomaterials for the abatement of pharmaceuticals and personal care products from wastewater, Appl. Sci. (Switz.) 8 (2018) 170, https://doi.org/10.3390/app8020170.

[44] A.F.M. Streit, G.C. Collazzo, S.P. Druzian, R.S. Verdi, E.L. Foletto, L.F.S. Oliveira, G.L. Dotto, Adsorption of ibuprofen, ketoprofen, and paracetamol onto activated carbon prepared from effluent treatment plant sludge of the beverage industry, Chemosphere 262 (2021) 128322, https://doi.org/10.1016/j.chemosphere.2020.128322.

[45] E. Moctezuma, E. Leyva, C.A. Aguilar, R.A. Luna, C. Montalvo, Photocatalytic degradation of paracetamol: intermediates and total reaction mechanism, J. Hazard. Mater. 243 (2012) 130–138, https://doi.org/10.1016/j.jhazmat.2012.10.010.

[46] D. Vogna, R. Marotta, A. Napolitano, M. D'Ischia, Advanced oxidation chemistry of paracetamol. UV/H_2O_2-induced hydroxylation/degradation pathways and 15N-aided inventory of nitrogenous breakdown products, J. Org. Chem. 67 (2002) 6143–6151, https://doi.org/10.1021/jo025604v.

[47] W. Xiao, J. Zhang, J. Wu, Recent advances in reactions involving carbon dioxide radical anion, ACS. Catal. 13 (2023) 15991–16011, https://doi.org/10.1021/acscatal.3c04125.

[48] B.K. Mutuma, G.N. Shao, W.D. Kim, H.T. Kim, Sol–gel synthesis of mesoporous anatase–brookite and anatase–brookite–rutile TiO_2 nanoparticles and their photocatalytic properties, J. Colloid. Interface Sci. 442 (2015) 1–7, https://doi.org/10.1016/j.jcis.2014.11.060.

[49] D. Alvira, D. Antorán, H. Darjazi, G.A. Elia, V. Sebastian, J.J. Manyà, Sustainable conversion of vine shoots and pig manure into high-performance anode materials for sodium-ion batteries, J. Power. Sources. 614 (2024), https://doi.org/10.1016/j.jpowsour.2024.235043.

[50] O. Üner, N. Aslan, A. Sarıoğlu, F. Semerci, M.M. Koç, Facile preparation of commercial Bi_2O_3 nanoparticle decorated activated carbon for pseudocapacitive supercapacitor applications, J. Mater. Sci.: Mater. Electron. 32 (2021) 15981–15994, https://doi.org/10.1007/s10854-021-06149-1.

[51] A. Chiadò, C. Novara, A. Lamberti, F. Geobaldo, F. Giorgis, P. Rivolo, Immobilization of oligonucleotides on metal-dielectric nanostructures for miRNA detection, Anal. Chem. 88 (2016) 9554–9563, https://doi.org/10.1021/acs.analchem.6b02186.

[52] Y. Hu, H.L. Tsai, C.L. Huang, Effect of brookite phase on the anatase-rutile transition in titania nanoparticles, J. Eur. Ceram. Soc. 23 (2003) 691–696, https://doi.org/10.1016/S0955-2219(02)00194-2.

[53] M. Piumetti, B. Bonelli, P. Massiani, S. Dzwigaj, I. Rossetti, S. Casale, M. Armandi, C. Thomas, E. Garrone, Effect of vanadium dispersion and of support properties on the catalytic activity of V-containing silicas, Catal. Today 179 (2012), https://doi.org/10.1016/j.cattod.2011.06.028.

[54] M. Armandi, B. Bonelli, E.I. Karaindrou, C.O. Areán, E. Garrone, Post-synthesis modifications of SBA-15 carbon replicas: improving hydrogen storage by increasing microporous volume, Catal. Today 138 (2008), https://doi.org/10.1016/j.cattod.2008.05.002.

[55] M. Kapilashrami, Y. Zhang, Y.-S. Liu, A. Hagfeldt, J. Guo, Probing the optical property and electronic structure of TiO_2 nanomaterials for renewable energy applications, Chem. Rev. 114 (2014) 9662–9707, https://doi.org/10.1021/cr5000893.

[56] T. Ohsaka, F. Izumi, Y. Fujiki, Raman spectrum of anatase, TiO_2, J. Raman Spectrosc. 7 (1978) 321–324, https://doi.org/10.1002/jrs.1250070606.

[57] J. Zhang, M. Li, Z. Feng, J. Chen, C. Li, UV raman spectroscopic study on TiO_2- I. phase transformation at the surface and in the bulk, J. Phys. Chem. B 110 (2006) 927–935, https://doi.org/10.1021/jp0552473.

[58] W. Hu, L. Li, G. Li, C. Tang, L. Sun, High-quality brookite TiO_2 flowers: synthesis, characterization, and dielectric performance, Cryst. Growth Des. 9 (2009) 3676–3682, https://doi.org/10.1021/cg9004032.

[59] H. Zhao, L. Liu, J.M. Andino, Y. Li, Bicrystalline TiO_2 with controllable anatase-brookite phase content for enhanced CO_2 photoreduction to fuels, J Mater Chem Mater 1 (2013) 8209–8216, https://doi.org/10.1039/c3ta11226h.

[60] P.P. Sarngan, A. Lakshmanan, D. Sarkar, Influence of anatase-rutile ratio on band edge position and defect states of TiO_2 homojunction catalyst, Chemosphere 286 (2022), https://doi.org/10.1016/j.chemosphere.2021.131692.

[61] C. Liu, F. Wang, J. Zhang, K. Wang, Y. Qiu, Q. Liang, Z. Chen, Efficient photoelectrochemical water splitting by g-C_3N_4/TiO_2 nanotube array heterostructures, Nanomicro Lett. 10 (2018) 1–13, https://doi.org/10.1007/s40820-018-0192-6.

[62] D. Hamdi, L. Mansouri, V. Srivastava, M. Sillanpaa, L. Bousselmi, Enhancement of Eu and Ce doped TiO_2 thin films photoactivity: application on Amido Black photodegradation, Inorg. Chem. Commun. 133 (2021), https://doi.org/10.1016/j.inoche.2021.108912.

[63] R. Katoh, K. Takahashi, K. Sugawa, Quantum yields of photoluminescence of TiO2Photocatalysts, J. Phys. Chem. C 126 (2022) 20954–20959, https://doi.org/10.1021/acs.jpcc.2c06761.

[64] N.D. Abazović, M.I. Čomor, M.D. Dramićanin, D.J. Jovanović, S.P. Ahrenkiel, J. M. Nedeljković, Photoluminescence of anatase and rutile TiO_2 particles, J. Phys. Chem. B 110 (2006) 25366–25370, https://doi.org/10.1021/jp064454f.

[65] H. Yaghoubi, Z. Li, Y. Chen, H.T. Ngo, V.R. Bhethanabotla, B. Joseph, S. Ma, R. Schlaf, A. Takshi, Toward a visible light-driven photocatalyst: the effect of midgap-states-induced energy gap of undoped TiO_2 nanoparticles, ACS. Catal. 5 (2015) 327–335, https://doi.org/10.1021/cs501539q.

[66] J. Li, Q. Zhang, J. Liu, M. Yu, H. Ma, J. Yang, S. Ye, T. Ramirez Reina, J. Liu, In-situ formation of carboxylate species on TiO_2 nanosheets for enhanced visible-light photocatalytic performance, J. Colloid. Interface Sci. 577 (2020) 512–522, https://doi.org/10.1016/j.jcis.2020.05.054.

[67] T. Umebayashi, T. Yamaki, H. Itoh, K. Asai, Analysis of electronic structures of 3d transition metal-doped TiO_2 based on band calculations, J. Phys. Chem. Solids 63 (2002) 1909–1920, https://doi.org/10.1016/S0022-3697(02)00177-4.

[68] J. Choi, H. Park, M.R. Hoffmann, Effects of single metal-ion doping on the visible-light photoreactivity of TiO_2, J. Phys. Chem. C 114 (2010) 783–792, https://doi.org/10.1021/jp908088x.

[69] R. Nakamura, T. Tanaka, Y. Nakato, Mechanism for visible light responses in anodic photocurrents at N-doped TiO_2 film electrodes, J. Phys. Chem. B 108 (2004) 10617–10620, https://doi.org/10.1021/jp048112q.

[70] X. Chen, L. Liu, P.Y. Yu, S.S. Mao, Increasing solar absorption for photocatalysis with black hydrogenated titanium dioxide nanocrystals, Science 331 (2011) 746–750, https://doi.org/10.1126/science.1200448, 1979.

[71] G. Liu, W. Jaegermann, J. He, V. Sundström, L. Sun, XPS and UPS characterization of the TiO_2/ZnPcGly heterointerface: alignment of energy levels, J. Phys. Chem. B 106 (2002) 5814–5819, https://doi.org/10.1021/jp014192b.

[72] C. Deiana, E. Fois, S. Coluccia, G. Martra, Surface structure of TiO_2 P25 nanoparticles: infrared study of hydroxy groups on coordinative defect sites, J. Phys. Chem. C 114 (2010) 21531–21538, https://doi.org/10.1021/jp107671k.

[73] A.L. Linsebigler, G. Lu, J.T. Yates, Photocatalysis on TiO_2 surfaces: principles, mechanisms, and selected results, Chem. Rev. 95 (1995) 735–758, https://doi.org/10.1021/cr00035a013.

[74] M.A. Henderson, Evidence for bicarbonate formation on vacuum annealed TiO_2 (110) resulting from a precursor-mediated interaction between CO_2 and H_2O, Surf. Sci. 400 (1998) 203–219, https://doi.org/10.1016/S0039-6028(97)00863-7.

[75] X. Tian, J. Mi, Z. Qian, L. Gan, H. Huang, J. Chen, J. Li, Inverse electronic state modulation of different metal sites in high-entropy oxides through constructing ultrathin sheet structure to boost NO reduction by CO, Appl. Catal. B 367 (2025), https://doi.org/10.1016/j.apcatb.2025.125115.

[76] L.H. Gao, W.Y. Xiao, M.Y. Qi, J.Y. Li, C.L. Tan, Z.R. Tang, Photoredox-catalyzed coupling of CO_2 reduction and amines oxidation by Cu doped CdS quantum dots, Mol. Catal. 554 (2024), https://doi.org/10.1016/j.mcat.2024.113858.

[77] C.-L. Tan, M.-Y. Qi, Z.-R. Tang, Y.-J. Xu, Superior photoredox coupling of selective ethanol oxidation and CO_2 reduction over $ZnIn_2S_x$@CeO_x with spatially separated redox active sites, Artif. Photosynth. 1 (2025) 144–155, https://doi.org/10.1021/aps.5c00005.

[78] L. Liu, H. Zhao, J.M. Andino, Y. Li, Photocatalytic CO_2 reduction with H_2O on TiO_2 nanocrystals: comparison of anatase, rutile, and brookite polymorphs and exploration of surface chemistry, ACS. Catal. 2 (2012) 1817–1828, https://doi.org/10.1021/cs300273q.

[79] L. Mino, G. Spoto, A.M. Ferrari, CO_2 capture by TiO_2 anatase surfaces: a combined DFT and FTIR study, J. Phys. Chem. C 118 (2014) 25016–25026, https://doi.org/10.1021/jp507443k.

[80] L.F. Liao, C.F. Lien, D.L. Shieh, M.T. Chen, J.L. Lin, FTIR study of adsorption and photoassisted oxygen isotopic exchange of carbon monoxide, carbon dioxide, carbonate, and formate on TiO_2, J. Phys. Chem. B 106 (2002) 11240–11245, https://doi.org/10.1021/jp0211988.

[81] A. Mattsson, L. Österlund, Adsorption and photoinduced decomposition of acetone and acetic acid on anatase, brookite, and rutile TiO_2 nanoparticles, J. Phys. Chem. C 114 (2010) 14121–14132, https://doi.org/10.1021/jp103263n.

[82] A. Litke, Y. Su, I. Tranca, T. Weber, E.J.M. Hensen, J.P. Hofmann, Role of adsorbed water on charge carrier dynamics in photoexcited TiO_2, J. Phys. Chem. C 121 (2017) 7514–7524, https://doi.org/10.1021/acs.jpcc.7b00472.

[83] M.S. Johnson, M. Ates, Z. Arslan, I.O. Farah, C. Bogatu, Assessment of crystal morphology on uptake, particle dissolution, and toxicity of nanoscale titanium dioxide on Artemia Salina, J. Nanotoxicol. Nanomed. 2 (2017) 11–27, https://doi.org/10.4018/jnn.2017010102.

[84] A. Mattsson, S. Hu, K. Hermansson, L. Österlund, Infrared spectroscopy study of adsorption and photodecomposition of formic acid on reduced and defective rutile TiO_2 (110) surfaces, J. Vac. Sci. Technol. A: Vac. Surf. Films 32 (2014), https://doi.org/10.1116/1.4898568.

[85] G.Y. Popova, T.V. Andrushkevich, Y.A. Chesalov, E.S. Stoyanov, In situ FTIR study of the adsorption of formaldehyde, formic acid, and methyl formiate at the surface of TiO_2 (anatase), Kinet. Catal. 41 (2000) 805–811, https://doi.org/10.1023/A:1026681321584.

[86] J. Raskó, F. Solymosi, Infrared spectroscopic study of the photoinduced activation of CO_2 on T_1O_2 and Rh/TiO_2, J. Phys. Chem. 98 (1994) 7147–7152. https://pubs.acs.org/sharingguidelines.

[87] J. Soria, J. Sanz, I. Sobrados, J.M. Coronado, M.D. Hernández-Alonso, F. Fresno, Water-hydroxyl interactions on small anatase nanoparticles prepared by the hydrothermal route, J. Phys. Chem. C 114 (2010) 16534–16540, https://doi.org/10.1021/jp105131w.

[88] H. Li, M. Vrinat, G. Berhault, D. Li, H. Nie, P. Afanasiev, Hydrothermal synthesis and acidity characterization of TiO_2 polymorphs, Mater. Res. Bull. 48 (2013) 3374–3382, https://doi.org/10.1016/j.materresbull.2013.05.017.

[89] J.P. Holmberg, E. Ahlberg, J. Bergenholtz, M. Hassellöv, Z. Abbas, Surface charge and interfacial potential of titanium dioxide nanoparticles: experimental and theoretical investigations, J. Colloid. Interface Sci. 407 (2013) 168–176, https://doi.org/10.1016/j.jcis.2013.06.015.

[90] K. Suttiponparnit, J. Jiang, M. Sahu, S. Suvachittanont, T. Charinpanitkul, P. Biswas, Role of surface area, primary particle size, and crystal phase on titanium dioxide nanoparticle dispersion properties, Nanoscale Res. Lett. 6 (2011) 1–8, https://doi.org/10.1007/s11671-010-9772-1.

[91] L. Yang, L.E. Yu, M.B. Ray, Degradation of paracetamol in aqueous solutions by TiO_2 photocatalysis, Water. Res. 42 (2008) 3480–3488, https://doi.org/10.1016/J.WATRES.2008.04.023.

[92] D.F. Ollis, Kinetics of photocatalyzed reactions: five lessons learned, Front. Chem. 6 (2018) 1–7, https://doi.org/10.3389/fchem.2018.00378.

[93] N. Blangetti, F.S. Freyria, M.C. Calviello, N. Ditaranto, S. Guastella, B. Bonelli, Photocatalytic degradation of paracetamol under simulated sunlight by four TiO_2 commercial powders: an insight into the performance of two sub-micrometric anatase and rutile powders and a nanometric brookite powder, Catalysts. 13 (2023) 434, https://doi.org/10.3390/catal13020434.

[94] T.M. Khedr, S.M. El-Sheikh, E. Kowalska, H.M. Abdeldayem, The synergistic effect of anatase and brookite for photocatalytic generation of hydrogen and diclofenac degradation, J. Environ. Chem. Eng. 9 (2021) 106566, https://doi.org/10.1016/j.jece.2021.106566.

[95] I.M. Raju, T.S. Rao, K.V.Di. Lakshmi, M.R. Chandra, J.S. Padmaja, G. DIvya, Poly 3-thenoic acid sensitized, copper doped anatase/brookite TiO_2 nanohybrids for enhanced photocatalytic degradation of an organophosphorus pesticide, J. Environ. Chem. Eng. 7 (2019), https://doi.org/10.1016/j.jece.2019.103211.

[96] N. Villota, J.M. Lomas, L.M. Camarero, Study of the paracetamol degradation pathway that generates color and turbidity in oxidized wastewaters by photo-Fenton technology, J. Photochem. Photobiol. Chem. 329 (2016) 113–119, https://doi.org/10.1016/j.jphotochem.2016.06.024.

[97] R. Cabrera-Alonso, E. Guevara, M.G. Ramírez-Elías, B. Moncada, F.J. González, Surface-enhanced Raman scattering of hydroquinone assisted by gold nanorods, J. Nanophotonics. 13 (2019) 1, https://doi.org/10.1117/1.jnp.13.036006.

[98] Z. Mukanova, K. Gudun, Z. Elemessova, L. Khamkash, E. Ralchenko, R. Bukasov, Detection of paracetamol in water and urea in artificial urine with gold nanoparticle@AI foil cost-efficient SERS substrate, Anal. Sci. 34 (2018) 183–187, https://doi.org/10.2116/analsci.34.183.

[99] N. Hao, M. Chen, H. Yang, R. Li, Q. Liu, Y. Zhu, L. Wang, M. Peng, J. Xiang, X. Chen, "pomegranate-like" plasmonic nanoreactors with accessible high-density hotspots for in situ SERS monitoring of catalytic reactions, Anal. Chem. 92 (2020) 4115–4122, https://doi.org/10.1021/acs.analchem.0c00069.

[100] C. De Bleye, E. Dumont, E. Rozet, P.Y. Sacré, P.F. Chavez, L. Netchacovitch, G. Piel, P. Hubert, E. Ziemons, Determination of 4-aminophenol in a pharmaceutical formulation using surface enhanced Raman scattering: from development to method validation, Talanta 116 (2013) 899–905, https://doi.org/10.1016/j.talanta.2013.07.084.

[101] A. Virga, P. Rivolo, F. Frascella, A. Angelini, E. Descrovi, F. Geobaldo, F. Giorgis, Silver nanoparticles on porous silicon: approaching single molecule detection in resonant SERS regime, J. Phys. Chem. C 117 (2013) 20139–20145, https://doi.org/10.1021/jp405117p.

[102] C. Novara, S. Dalla Marta, A. Virga, A. Lamberti, A. Angelini, A. Chiadò, P. Rivolo, F. Geobaldo, V. Sergo, A. Bonifacio, F. Giorgis, SERS-active Ag nanoparticles on porous silicon and PDMS substrates: a comparative study of uniformity and Raman efficiency, J. Phys. Chem. C 120 (2016) 16946–16953, https://doi.org/10.1021/acs.jpcc.6b03852.

[103] C. Novara, D. Montesi, S. Bertone, N. Paccotti, F. Geobaldo, M. Channab, A. Angelini, P. Rivolo, F. Giorgis, A. Chiadò, Role of probe design and bioassay configuration in surface enhanced raman scattering based biosensors for miRNA detection, J. Colloid. Interface Sci. 649 (2023) 750–760, https://doi.org/10.1016/j.jcis.2023.06.090.

[104] C. Novara, A. Chiadò, N. Paccotti, S. Catuogno, C.L. Esposito, G. Condorelli, V. De Franciscis, F. Geobaldo, P. Rivolo, F. Giorgis, SERS-active metal-dielectric nanostructures integrated in microfluidic devices for label-free quantitative detection of miRNA, Faraday Discuss. 205 (2017) 271–289, https://doi.org/10.1039/c7fd00140a.

[105] J. Hu, J.K. Bi, C. Sun, Z. Men, Pressure-induced Fermi resonance between fundamental modes in α-hydroquinone, Spectrochim. Acta Mol. Biomol. Spectrosc. 299 (2023), https://doi.org/10.1016/j.saa.2023.122863.

[106] X.H. Pham, E. Hahm, K.H. Huynh, H.M. Kim, B.S. Son, D.H. Jeong, B.H. Jun, Sensitive and selective detection of 4-aminophenol in the presence of acetaminophen using gold–silver core–shell nanoparticles embedded in silica nanostructures, J. Ind. Eng. Chem. 83 (2020) 208–213, https://doi.org/10.1016/j.jiec.2019.11.030.

[107] E. Ashok Kumar, N. Riswana Barveen, T.J. Wang, T. Kokulnathan, Y.H. Chang, Development of SERS platform based on ZnO multipods decorated with Ag nanospheres for detection of 4-nitrophenol and rhodamine 6G in real samples, Microchem. J. 170 (2021) 106660, https://doi.org/10.1016/J.MICROC.2021.106660.

[108] C.L. Jahncke, W. Zhang, B.M. Demuynck, A.D. Hill, Exploring resonance Raman scattering with 4-nitrophenol, J. Chem. Educ. 99 (2022) 3233–3241, https://doi.org/10.1021/acs.jchemed.2c00210.

[109] S. Duraipandian, M.M. Knopp, M.R. Pollard, H. Kerdoncuff, J.C. Petersen, A. Müllertz, A fast and novel internal calibration method for quantitative Raman measurements on aqueous solutions, Anal. Methods 10 (2018) 3589–3593, https://doi.org/10.1039/c8ay00753e.

[110] B.A. Kolesov, Raman spectra of crystalline secondary amides, Spectrochim. Acta Mol. Biomol. Spectrosc. 179 (2017) 216–220, https://doi.org/10.1016/j.saa.2017.02.046.
[111] N. Riswana Barveen, T.J. Wang, Y.H. Chang, Photochemical synthesis of Ag/Au/AgCl heterostructure from Ag nanowires as a reusable SERS substrate for ultrasensitive detection of analgesics and antibiotics, Chem. Eng. J. 423 (2021), https://doi.org/10.1016/j.cej.2021.130191.
[112] R. Cabrera-Alonso, E. Guevara, M.G. Ramírez-Elías, B. Moncada, F.J. González, Detection of hydroquinone by Raman spectroscopy in patients with melasma before and after treatment, Skin Res. Technol. 25 (2019) 20–24, https://doi.org/10.1111/srt.12589.
[113] N.S. Powar, S. Kim, J. Lee, E. Gong, C.B. Hiragond, D. Kim, T. Zhang, M. Kim, S. Il In, Unravelling the effect of Ti^{3+}/Ti^{3+} active sites dynamic on reaction pathways in direct gas-solid-phase CO_2 photoreduction, Appl. Catal. B 352 (2024), https://doi.org/10.1016/j.apcatb.2024.124006.
[114] Y. Bai, M. Li, X. Liu, J. Han, X. Zhu, Q. Ge, H. Wang, Ti^{3+} defective TiO_2/CdS Z-scheme photocatalyst for enhancing photocatalytic CO_2 reduction to C1-C3 products, Ind. Eng. Chem. Res. 61 (2022) 8724–8737, https://doi.org/10.1021/acs.iecr.2c01113.
[115] S. Rana, A. Kumar, G. Sharma, P. Dhiman, A. García-Penas, F.J. Stadler, Recent advances in perovskite-based Z-scheme and S-scheme heterojunctions for photocatalytic CO_2 reduction, Chemosphere 339 (2023), https://doi.org/10.1016/j.chemosphere.2023.139765.
[116] L. Yuan, M.Y. Qi, Z.R. Tang, Y.J. Xu, Coupling strategy for CO_2 valorization integrated with organic synthesis by heterogeneous photocatalysis, Angew. Chem. - Int. Ed. 60 (2021) 21150–21172, https://doi.org/10.1002/anie.202101667.